Technical University of Munich
School of Engineering and Design
Deutsches Geodätisches Forschungsinstitut (DGFI-TUM)
Prof. Dr.-Ing. habil. Florian Seitz

Combined precise orbit determination of Jason-3 based on SLR and DORIS observations

Baumgartner, Miriam

Master's Thesis

Study program Geodesy and Geoinformation

Supervisor(s) Dr.-Ing. Mathis Bloßfeld
Deutsches Geodätisches Forschungsinstitut (DGFI-TUM)
Technical University of Munich

M.Sc. Julian Zeitlhöfler
Deutsches Geodätisches Forschungsinstitut (DGFI-TUM)
Technical University of Munich

December 7, 2025

Declaration of Authorship

I confirm that this Master's thesis is my own work and I have documented all sources and material used.

This thesis was not previously presented to another examination board and has not been published.

Munich, December 7, 2025, Signature

Abstract

The Genesis mission, launching in 2028, aims to collocate the four space-geodetic techniques Doppler Orbitography and Radiopositioning Integrated by Satellite (DORIS), Global Navigation Satellite System (GNSS), Satellite Laser Ranging (SLR), and Very Long Baseline Interferometry (VLBI) within a single satellite platform. To validate multi-technique precise orbit determination (POD) strategies prior to launch, the Jason-3 satellite, carrying three of the four space-geodetic techniques, serves as a suitable test platform. Within the Genesis-D project, DGFI-TUM is responsible for evaluating SLR and DORIS. Consequently, the validation of a combined SLR/DORIS POD solution is performed using Jason-3 data.

For a selected mission period, the optimal relative weighting of SLR and DORIS observations, as well as the corresponding parameter setup, is determined and analyzed through a combined POD at observation level. Initial tests on the first 200 arcs, with an arc length of 3.5 days, are conducted to analyze the structural behavior of weighting schemes. The optimal setup is first determined for the initial arc and then applied to 14 overlapping three-day arcs during a phase with a high number of SLR observations. Subsequently, these optimized settings are applied to the entire time span covered by the 200 arcs to evaluate the resulting improvement over the full analysis period.

A comprehensive evaluation of the obtained relative weights is performed. The final solution is assessed through a combined evaluation using internal validation (orbit parameters, stochastic properties, and overlap differences) and external validation (comparisons with reference orbits). The reference orbits from CNES and JPL initially serve as directional benchmarks, while the GSFC orbit, released only in the late stage of this thesis, is incorporated as an additional comparison into the external validation. The joint internal-external validation process yields final technique-specific standard deviations of 0.2 mm/s for DORIS and 5 cm for SLR.

Zusammenfassung

Die Genesis-Mission, deren Start für 2028 geplant ist, verfolgt das Ziel, die vier geodätischen Raumverfahren Doppler Orbitography and Radiopositioning Integrated by Satellite (DORIS), Global Navigation Satellite System (GNSS), Satellite Laser Ranging (SLR) und Very Long Baseline Interferometry (VLBI) auf einer Satellitenplattform zu vereinen. Um eine präzise Orbitbestimmung (POD) mehrerer Techniken vor dem Missionsstart zu validieren, dient der Jason-3 Satellit als geeignete Testplattform, da sich drei der vier geodätischen Raumverfahren an Bord befinden. Im Rahmen des Genesis-D-Projekts ist das DGFI-TUM für die Auswertung von SLR sowie DORIS verantwortlich. Entsprechend wird die Validierung einer kombinierten SLR/DORIS-POD-Lösung unter Verwendung von Beobachtungen zu Jason-3 durchgeführt.

Für einen ausgewählten Missionszeitraum wird durch eine kombinierte POD auf Beobachtungsebene die optimale relative Gewichtung der SLR- und DORIS-Messungen sowie das zugehörige Parametersetup bestimmt und analysiert. Erste Tests an 200 Bögen der Mission, mit einer Bogenlänge von 3.5 Tagen, werden durchgeführt, um das strukturelle Verhalten verschiedener Gewichtungsschemata zu analysieren. Die optimale Konfiguration wird zunächst für den ersten Bogen der Mission bestimmt und anschließend auf 14 überlappende drei-Tages-Bögen in einer Phase mit einer hohen Anzahl an SLR-Beobachtungen angewendet. Anschließend werden die gefundenen Einstellungen auf den gesamten Zeitraum angewendet, der durch die 200 Bögen abgedeckt wird, um die erzielte Verbesserung über den vollständigen Analysezeitraum zu bewerten.

Eine umfassende Bewertung der bestimmten relativen Gewichte wird durchgeführt und die endgültige Lösung wird sowohl mittels interner Kriterien (Orbitparameter, stochastische Eigenschaften und Überlappungsdifferenzen) als auch durch externe Validierung anhand von Referenzorbits beurteilt. Die Referenzorbits von CNES und JPL dienen zunächst als Vergleichsgrundlage, während der Orbit von GSFC, der erst in einer späten Phase dieser Arbeit veröffentlicht wurde, als zusätzlicher Vergleich in die externe Validierung einbezogen wird. Die endgültigen, technikspezifischen Standardabweichungen, 0.2 mm/s für DORIS sowie 5 cm für SLR, ergeben sich aus dem kombinierten Prozess aus interner und externer Validierung.

Contents

1 Introduction **1**

2 Theory **5**

2.1 Satellite Laser Ranging 5

2.1.1 Principle of SLR 5

2.1.2 Range corrections 6

2.1.3 Limitations 7

2.2 Doppler Orbitography and Radiopositioning Integrated by Satellite 8

2.2.1 System architecture 9

2.2.2 Doppler Observation Model 10

2.2.3 Limitations 11

2.3 Jason-3 satellite 12

2.3.1 Mission objectives 12

2.3.2 Orbit characteristics 12

2.3.3 Payload 12

2.3.4 Mission products 13

2.4 Precise orbit determination 13

2.4.1 Principle 14

2.4.2 State of the art 15

2.5 Orbit perturbations 15

2.5.1 Gravitational perturbations 16

2.5.2 Non-gravitational perturbations 16

2.5.3 Other perturbations 17

2.6 Parameter estimation 18

2.6.1 Combination Strategies 20

2.6.2 Equation system for combined paramter estimation 20

2.6.3 Estimation of unknown parameters 22

3 Single- and multi-technique POD **23**

3.1 POD in DOGS-OC 24

3.1.1 General parameters 24

3.1.2 Perturbation Modelling 25

3.2 Test scenarios 26

3.2.1 Orbit parameter constraints 29

3.2.2 Relative weighting of DORIS and SLR 30

3.3 Orbit validation 34

3.3.1 Solution characteristics 35

3.3.2 Orbit parameter validation: internal validation 35
3.3.3 Orbit parameter validation: external validation 37
3.4 Derived settings for multi-technique POD 39
4 Results and discussion 41
4.1 Internal validation 41
4.1.1 Physical parameters 41
4.1.2 Biases 43
4.1.3 Statistical information 45
4.1.4 Orbit overlaps 47
4.2 External validation 49
5 Conclusion and outlook 57

Acronyms 60

List of Figures 62

List of Tables 62

Bibliography 63

1 Introduction

Space-geodetic techniques are essential for precisely measuring the Earth's shape, rotation, and gravitational field. These techniques form the backbone of the ITRF (International Terrestrial Reference Frame), which provides a consistent coordinate system for monitoring global geophysical phenomena, such as tectonic processes and changes in global sea level (Angermann et al., 2022). DORIS (Doppler Orbitography and Radiopositioning Integrated by Satellite), GNSS (Global Navigation Satellite System), SLR (Satellite Laser Ranging), and VLBI (Very Long Baseline Interferometry) each contribute unique and complementary information to the determination of Earth reference frames (Altamimi et al., 2016).

The ITRF serves as the standard terrestrial reference frame recommended by several international scientific organizations, including the IUGG (International Union of Geodesy and Geophysics) and the IAG (International Association of Geodesy), for applications in Earth science, satellite navigation, and positioning (International Union of Geodesy and Geophysics, 2007). It provides the basis for precise positioning on Earth and in space and enables reliable quantification of geodynamic processes and climate-related changes. Moreover, it is indispensable for understanding Earth dynamics, monitoring climate phenomena and operating natural hazard early-warning systems. The realization of the ITRF relies on the four space-geodetic techniques DORIS, GNSS, SLR and VLBI, each contributing observation records spanning several decades (GGOS, 2023). The four IAG services IVS (International VLBI Service for Geodesy and Astronomy, Nothnagel et al. (2017)), ILRS (International Laser Ranging Service, M. R. Pearlman et al. (2019)), IGS (International GNSS Service, Johnston et al. (2017)), and IDS (International DORIS Service, Willis et al. (2016)), analyze long-term observation data and provide technique-specific solutions. These individual solutions are combined by the three official ITRS (International Terrestrial Reference System) combination centers of the IERS (International Earth Rotation and Reference Systems Service), IGN (Institut national de l'information géographique et forestière), located in France, DGFI-TUM (Deutsches Geodätisches Forschungsinstitut) in Germany, and JPL (Jet Propulsion Laboratory) in the United States of America, to generate a consistent terrestrial reference frame (GGOS, 2023). The most recent realization, ITRF2020, was released in April 2022 (Altamimi et al., 2023).

In addition to the ITRF2020 realization, two further solutions, the DTRF2020 (The ITRS2020 realization of DGFI-TUM) and JTRF2020 (JPL Terrestrial Reference Frame 2020), were generated by the other ITRS Combination Centers (Gross et al., 2023; Seitz et al., 2023). The ITRF2020 and DTRF2020 follow the conventional secular approach, providing station positions at a reference epoch together with linear velocities, whereas JTRF2020 represents station coordinates as a time series derived from a Kalman filter. The secular frames also differ in their combination strategies and in the treatment of nonlinear station motions: the ITRF2020 combines at the solution level, while DTRF2020 combines normal equation systems and incorporates geophysical loading models. All secular frames include postseismic deformation models (Angermann et al., 2024).

The long-term origin of the ITRF is realized by SLR, while its scale results from a combination of the intrinsic scales of SLR and VLBI. Since both techniques are still affected by systematic errors and technical limitations, e.g., timing and range deviations in SLR or antenna deformations in VLBI, further improvements in their consistency are needed. Moreover, consistency in the orientation and temporal evolution of the ITRF across successive realizations must be maintained. To fulfill future scientific objectives related to the variability of the Earth system, its accuracy and long-term stability require improvement by at least one order of magnitude (Delva et al., 2025).

POD (Precise orbit determination) is essential for Earth observation missions, as the accuracy of the satellite's position directly affects the geophysical parameters derived from the observations, such as sea-level height in altimetry missions. While coarse orbit knowledge may be sufficient for operational purposes, remote sensing satellites require orbit accuracies several orders of magnitude higher. Earth observation instruments can achieve the spatial and geolocation accuracy required for scientific and geophysical applications only with a consistently precise orbit solution (Montenbruck & Gill, 2000). Furthermore, POD provides the foundation for combining multiple space-geodetic techniques within a unified reference frame, thereby supporting the realization and maintenance of the ITRF.

To address these challenges and to strengthen the consistency among the four space-geodetic techniques, ESA (European Space Agency) initiated the Genesis mission as a dedicated effort to enhance the global geodetic infrastructure. Scheduled for launch in 2028 (Gidlund, 2024), Genesis aims to integrate SLR, GNSS, DORIS, and VLBI on a single satellite platform (Honoré-Livermore, 2024). By co-locating these techniques in space, the mission aims to overcome the limitations of separate ground-based networks (Hugentobler, 2024) and enhance the accuracy and consistency of the ITRF (Gidlund, 2024). This integration is crucial for advancing Earth system research, enabling more accurate monitoring of geodynamic processes, sea-level rise, and crustal deformation. One of the mission's core objectives is to contribute to the ITRF parameter accuracy to 1 mm and its long-term stability to 0.1 mm/year, directly supporting the goals of GGOS (Global Geodetic Observing System) and the United Nations General Assembly Resolution 69/266 on the Global Geodetic Reference Frame for Sustainable Development (Fusco & Waller, 2025; United Nations General Assembly, 2015). GGOS, as part of IAG, coordinates the international geodetic infrastructure and sets accuracy targets for the realization of the ITRF (GGOS, 2025). As highlighted by Vespe and Karatekin (2025), a key component of Genesis is the combined use of all space-geodetic techniques for POD.

According to Vespe and Karatekin (2025), the benefits of the Genesis mission extend across several scientific fields. In geodesy, the mission aims to improve the ITRF, harmonize reference frames, and improve the determination of Earth rotation parameters. For navigation, more accurate GNSS orbits and position determinations, refined antenna phase center calibration, and advances in the precise orbit determination of satellites in near-Earth orbit are expected. In the geosciences, the mission contributes to a better understanding of climate processes such as sea level rise, ice mass loss, and climatology, as well as to the monitoring of the solid Earth, including tectonic movements, tidal and crustal deformations, and the prediction of natural hazards. In addition, Genesis supports tests of general relativity in the field of fundamental physics, for example, through investigations of gravitational redshift, pericenter precession, the Sagnac effect, and gravitomagnetic phenomena such as the Lense-Thirring effect.

Courde et al. (2025) report that Genesis introduces a new requirement for SLR: a laser range correction accuracy of 0.5 mm (1σ), which is an order of magnitude more stringent than for previous missions such as LAGEOS or LARES-2, achieving 5 mm and 2 mm, respectively. Achieving this level of precision requires an exceptionally calibrated retroreflector system and accurate knowledge of the satellite's center of mass. Furthermore, all geodetic techniques will be jointly calibrated on the satellite platform before launch.

DORIS, provides continuous Doppler-based measurements that are valuable for long-term tracking of station positions and Earth rotation parameters. However, its use on Genesis presents new technical challenges. The mission will fly a modified DGXX-S DORIS receiver, originally designed for low-Earth orbit (LEO), at an altitude of 6000 km in medium-Earth orbit (MEO), well beyond its nominal range. This results in longer signal paths, Doppler collisions and the need to select a subset of beacons visible at any given time. Additionally, the harsh radiation environment, particularly called the South Atlantic Anomaly, poses a risk to the stability of the onboard oscillator. This is due to the non-homogeneous nature of Earth's magnetic field, whose weakest region lies over the South Atlantic. As a result, the inner Van Allen radiation belt dips closer to Earth in this area, leading to significantly elevated particle densities, especially of high-energy protons, which are several orders of magnitude higher than in other parts of low-Earth and medium-Earth orbit. As a mitigation strategy, Genesis will use a GNSS-driven USO (Ultra Stable Oscillator) external to the DORIS unit (Moreaux et al., 2025).

The Genesis-D project was initiated by DLR (German Aerospace Center) to support the national contribution to ESA's Genesis mission. The project focuses on the realization of a four-technique space tie, enabling consistent processing, combination, and validation of Genesis observations across German institutions. Further objectives include the generation of uniform solutions from DORIS, GNSS, SLR, and VLBI for the realization of terrestrial and celestial reference frames as well as Earth orientation parameters, the extension of the SINEX format for orbit parameters and the development of strategies for integrating Genesis data into reference frame computation. Additionally, the project involves software extensions at BKG (Federal Agency for Cartography and Geodesy), DGFI-TUM, and GFZ (German Research Centre for Geosciences), along with simulations and real-data analyses using current co-location satellites and observation scheduling for SLR and VLBI (Altamimi & Seitz, 2025).

To validate multi-technique POD strategies prior to the launch of the Genesis mission, the Jason-3 satellite, carrying three of the four space-geodetic techniques SLR, DORIS, and GPS (Global Positioning System) (instead of GNSS), provides an ideal platform. In this context, it serves as a testbed for preparing and verifying the DGFI-TUM software framework for combined precise orbit determination. Given DGFI-TUM's responsibility for the evaluation of SLR and DORIS within the Genesis project, the validation of the combined SLR and DORIS POD solution is evaluated using Jason-3 as a reference satellite.

A multi-technique POD represents the simultaneous adjustment of measurements from multiple space-geodetic techniques within a common estimation framework. In this study, combined POD solutions are generated and analyzed at DGFI-TUM, focusing on the integration of SLR and DORIS observations. So far, no multi-technique solution has been realized within the DGFI-TUM processing framework, which makes this work an important first step toward such an implementation. The quality of the resulting orbit solutions is assessed using statistical parameters, including the RMS (root mean square), mean, and median of orbit differences. Beyond these statistical measures, the physical correctness of an orbit solution must also be ensured. This requires that all estimated parameters are consistent with each other and reflect realistic satellite dynamics to ensure that the resulting orbit solution remains physically meaningful.

In this context, the following research question is addressed in this thesis:

> **How can SLR and DORIS observations be relatively weighted, and how should the parameter setup be chosen, to obtain a reliable satellite orbit solution?**

A reliable satellite orbit is understood as an orbit solution that is physically meaningful and consistent with the available observations, exhibiting an adequate level of statistical quality.

To address this question, the thesis is structured as follows: Chapter 2 introduces the theoretical background, including SLR, DORIS, and the principles of POD with parameter estimation and orbit perturbations. Chapter 3 describes the setup for the multi-technique POD, followed by the evaluation and discussion of the results in Chapter 4. The thesis concludes with a summary and outlook in Chapter 5.

2 Theory

This chapter outlines the theoretical foundations relevant to this study. It introduces the space-geodetic techniques SLR and DORIS, describes the Jason-3 satellite, and discusses orbit perturbations and parameter estimation within the context of POD.

2.1 Satellite Laser Ranging

SLR has been in development since the early 1960s, with the first successful satellite tracking experiments conducted by NASA (National Aeronautics and Space Administration) as part of the Beacon B mission in 1964 (Smith, 1964, cited in Combrinck, 2010). Over the decades, the technology has evolved from meter-level accuracy in its early years to a current accuracy of about one to two centimeters. SLR offers an opportunity to monitor slowly varying geodynamic processes on Earth as well as temporal changes in the long-wave components of the gravitational field. It also makes a significant contribution to the realization of the ITRF and is used for the calibration and validation of other satellite techniques. Since SLR satellites have a long operational life, they enable longer observation periods and are considered stable, long-term scientific instruments (Combrinck, 2010).

The international service responsible for this technique is the ILRS (International Laser Ranging Service), which is in charge of collecting, merging, analyzing, archiving, and distributing SLR and LLR (Lunar Laser Ranging) observation data sets (M. R. Pearlman et al., 2002), and ensures the global continuity of these measurements through its international network of ground stations (Combrinck, 2010). At this point, the author acknowledges the open data policy of the ILRS (M. R. Pearlman et al., 2019). As of 2025, the worldwide network of SLR stations comprises 39 operational SLR stations distributed worldwide (IAG, 2025; ILRS, 2025).

2.1.1 Principle of SLR

In essence, the fundamental principle of SLR can be summarized as follows: it determines the distance to satellites equipped with retroreflectors by measuring the round-trip travel time of short laser pulses, from which the range is calculated with very high precision (Montenbruck & Gill, 2000).

SLR satellites are equipped with retroreflectors and are tracked by ground-based optical telescopes that transmit laser pulses, which are reflected from the satellite. A time interval counter in the telescope is triggered by both the emission and reception of these pulses, and the returning signal is detected by a sensitive photodetector, providing the stop signal for the counter. This process enables precise range determination based on the laser pulse's time-of-flight (Combrinck, 2010; M. R. Pearlman et al., 2002). Equation 2.1 shows the basic formula for the SLR range measurement with

ρ being the measured range, c the speed of light, and Δt the two-way travel time.

$$\rho = c \cdot \frac{\Delta t}{2} \tag{2.1}$$

Figure 1 gives a schematic overview of the measurement principle, highlighting the sent and received laser pulse in red, the determined time difference in green, and the corrections to be adjusted in blue. The measured time distance (divided by 2) is then converted into the range, marked as distance ρ in the figure.

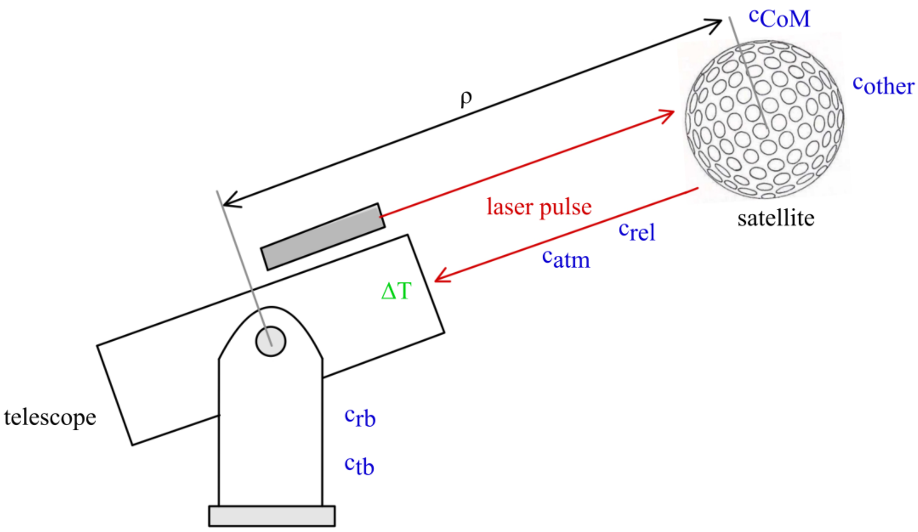

Figure 1 Schematic overview of SLR measurement principle, illustration based on Lösler et al. (2021) and Zeitlhöfler (2019), modified by the author. Satellite image taken from NASA Goddard Space Flight Center (1976).

SLR is uniquely sensitive to the Earth's center of mass and therefore plays a primary role in determining geocenter motion. Analyses of SLR data provide not only precise satellite orbits and station coordinates, but also fundamental geodetic parameters such as geocenter variations, polar motion, and Earth rotation parameters (Vermaat et al., 1998).

2.1.2 Range corrections

According to Combrinck (2010), several range corrections must be applied. The range equation 2.1 must be extended to include correction terms, such as the atmospheric delay correction c_{atm}, the center-of-mass correction c_{CoM}, station range bias c_{rb} and time bias c_{tb}, the relativistic range correction c_{rel} and additional yet unknown corrections c_{other}, resulting in

$$\rho = c \cdot \frac{\Delta t}{2} + c_{\text{atm}} + c_{\text{CoM}} + c_{\text{rb}} + c_{\text{tb}} + c_{\text{rel}} + c_{\text{other}} \cdot \tag{2.2}$$

Variations in the atmospheric refractive index affect the laser pulse by altering its group velocity and causing ray bending. These effects introduce systematic range errors of several meters, particularly at low elevation angles. Although atmospheric models using local meteorological data can correct most of this bias, residual errors remain in the centimeter range (Degnan, 1993). The corresponding correction term, denoted as c_{atm} in equation 2.2, accounts for these atmospheric effects.

The laser pulse is reflected from the satellite's surface rather than a precisely defined point. Since this reflection point does not coincide with the satellite's center of mass, the returned pulse experiences slight temporal spreading due to varying reflection geometries. Consequently, a center-of-mass correction c_{CoM} must be applied to the measured range. The corresponding correction values are provided by the ILRS (Combrinck, 2010).

Range biases c_{rb} in SLR represent a correction that must be applied to account for small but persistent errors in the measured range. While the term is often referred to as a station range bias, it does not always correspond to a real, physical error at the station itself; rather, it can also arise computationally during data processing. Range biases can result from several sources, including nonlinearities in the timing electronics, inaccuracies in atmospheric parameters (pressure, temperature, humidity) affecting the delay model, or miscalibration between the telescope reference point and the station's geodetic reference point. A positive range bias means that the measured range is too long and must be reduced, whereas a negative bias indicates an underestimated distance. Biases may also vary due to differences in signal strength, calibration instability, or varying analysis strategies across processing centers. Since range biases are correlated with the station's vertical position, it can be difficult to separate them from coordinate errors, and they are usually estimated as an additional parameter during the least-squares adjustment of observed minus computed residuals (Combrinck, 2010).

A time deviation c_{tb} in SLR arises from discrepancies between the station clock and Coordinated Universal Time (UTC). This so-called time tag error causes a shift in the epoch in which the observations are recorded. The satellite may appear ahead of or behind its expected orbital position, depending on the sign. Highly stable oscillators and accurate time measuring devices are required to minimize such errors, with optical time interval devices and master oscillators providing precise clock pulses for the measuring system (Degnan, 1993).

Additionally, a relativistic range correction c_{rel} must be applied. More details are found in Combrinck (2010) and McCarthy and Petit (2004). Since there are yet some unknown or undetermined error sources, these are represented by adding c_{other}.

2.1.3 Limitations

SLR systems emit green laser light at a wavelength of 532 nm in ultra-short pulses ranging from 30 ps to 200 ps, typically at repetition rates between 5 Hz and 10 Hz. In contrast to radar systems, laser tracking cannot autonomously acquire or follow satellites; it requires precise a priori orbital information for accurate pointing. Furthermore, the technique is restricted by meteorological conditions and operational constraints of the ground segment (Montenbruck & Gill, 2000). Since clear-sky conditions are essential for reliable measurements, stations must be located in regions with generally favorable weather (UTA, 2025). Another limiting factor is the unequal geographical distribution of stations between the northern and southern hemispheres (Sośnica et al., 2015).

Figure 2 illustrates the distribution of the SLR stations and DORIS beacons used for POD in Chapter 3. The station coordinates are taken from SLRF2020 (Satellite Laser Ranging Frame 2020) and DPOD2020 (DORIS extension of the ITRF for Precise Orbit Determination) 4.0 (Moreaux et al., 2023; Pavlis & Luceri, 2022).

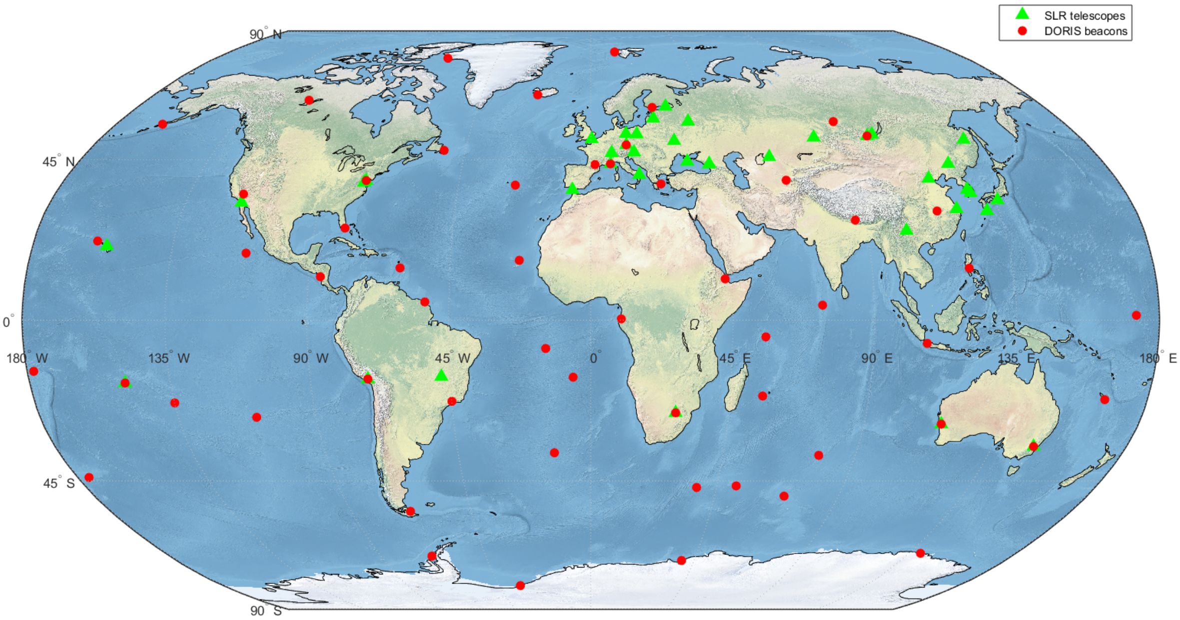

Figure 2 Global distribution of SLR stations and DORIS beacons.

2.2 Doppler Orbitography and Radiopositioning Integrated by Satellite

The DORIS system was developed in the late 1980s by CNES (Centre National d'Études Spatiales), IGN, and GRGS (Groupe de Recherche de Géodésie Spatiale) to support satellite altimetry missions (Jayles et al., 2006). It was initially developed to enable high-precision orbit determination for low Earth orbit satellites, primarily to support the ocean altimetry mission of the TOPEX/Poseidon satellite, which was in operation from 1992 until late 2005 (Auriol & Tourain, 2010). The IDS (International DORIS Service), as the international service of the system, archives and distributes DORIS data to the scientific community, while the beacon network is jointly managed by CNES and IGN (CNES, 2023; Willis et al., 2016). At this point, the author acknowledges the open data policy of the IDS (Willis et al., 2016).

2.2.1 System architecture

DORIS comprises three main segments: a global ground network, a space segment, and a processing center (Jayles et al., 2006). A schematic overview is given in Figure 3.

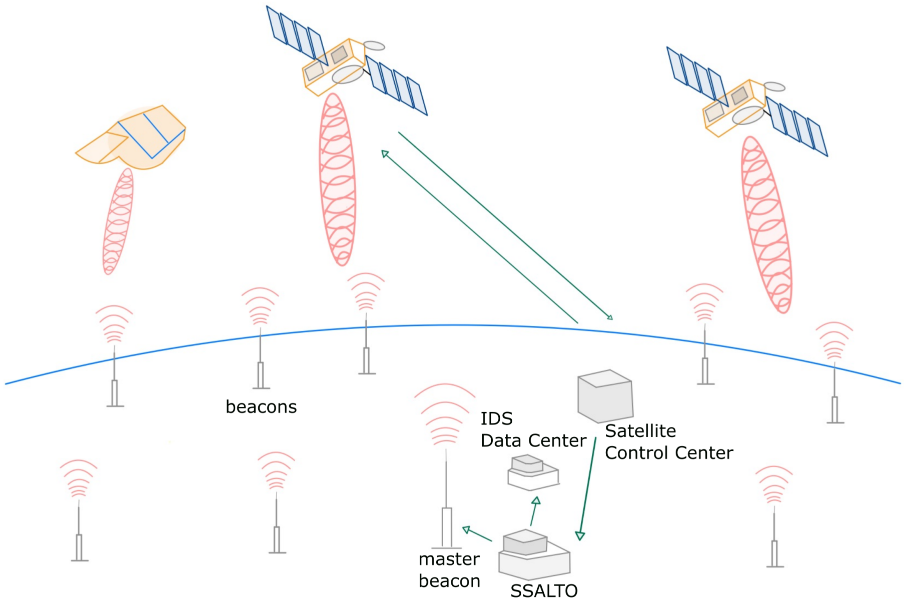

Figure 3 Schematic overview of DORIS segments and measurement principle, illustration based on CNES (2023).

The ground network comprises approximately 60 dual-frequency beacons transmitting at 2.03625 GHz and 401.25 MHz (IDS, 2025; Jayles et al., 2006). The higher frequency is used to determine the Doppler effect precisely, while the lower frequency allows ionospheric delay mitigation (Jayles et al., 2006). In 2013, 38 DORIS stations were co-located with other space-geodetic techniques, VLBI, SLR, and GNSS, enabling intercalibrations between the different space-geodetic techniques (IDS, 2025). Each beacon broadcasts identity, status, meteorological data, and synchronization information. Uplink transmissions allow fully automated beacon operations, including time-tagging, onboard storage, and transmission of real-time products with minimal ground intervention. In addition, so-called master beacons transmit broadcast uploads generated by the SSALTO (Segment Sol multi-mission Altimétrie, Orbitographie et Localisation Précise) ground segment. These contain essential information about the network, such as precise beacon coordinates, time ties, and time correspondence parameters, which are then used by the onboard receivers (Jayles et al., 2006).

Satellites carrying DORIS receivers form the space segment. The DORIS system analyzes Doppler shifts in radiofrequency signals transmitted from ground beacons and received onboard satellites (CNES, 2023). Each satellite uses its own time scale, synchronized with the stable onboard USO, whose behavior is monitored in real time and through detailed post-processing (Jayles et al., 2006). Later receiver generations also perform phase and delta-phase tracking, reaching sub-millimeter-per-second noise levels. The DIODE onboard software provides near real-time orbit determination with better than 1 m RMS accuracy, enabling autonomous navigation (Jayles et al., 2006).

Several ground facilities ensure data management and system operations. The IDS Data Centers are responsible for archiving and distributing DORIS measurements to the scientific community, while the Satellite Control Center manages spacecraft operations, including the downlink of DORIS telemetry and the uplink of commands such as software updates or parameter changes. The SSALTO multi-mission center, located in Toulouse, performs the main data processing tasks: it monitors system health, generates precise orbits, and processes measurements (CNES, 2023; Jayles et al., 2006).

The DORIS system provides several products: precise orbit ephemerides (1–3 cm accuracy), long-term ground station coordinate series, geophysical data on the ionosphere, troposphere, and geocenter motion, as well as near real-time orbit products for ocean monitoring and satellite operations. Since 1994, DORIS has contributed to the ITRF, with long-lived and stable stations that are particularly valuable for monitoring vertical crustal motion and sea-level rise (Jayles et al., 2006).

2.2.2 Doppler Observation Model

Beyond the system description, the mathematical observation model is essential for precise orbit determination. According to IDS Data Center, 2020, the DORIS system is based on coherent signals emitted by ground beacons and received by a spaceborne antenna. The primary observable is the Doppler count, which represents the difference in phase cycles between the emitted and received signals over a given time interval. This provides information about the line-of-sight velocity between the satellite and the beacon. With N_e as the emitted number of cycles and N_r the number of cycles generated by the receiver oscillator, the Doppler count is defined as

$$N_{\mathsf{DOP}} = N_\mathsf{e} - N_\mathsf{r} = f_\mathsf{e} \cdot \Delta\tau_\mathsf{e} - f_\mathsf{r} \cdot \Delta\tau_\mathsf{r}, \tag{2.3}$$

where f_e and f_r are the proper frequencies of the emitter and receiver, respectively, and $\Delta\tau_\mathsf{e}$, $\Delta\tau_\mathsf{r}$ are the proper time intervals of emission and reception. In practice, the Doppler count is derived from the phase difference between two epochs in the receiver's proper time, as stored in RINEX-DORIS files.

Relativistic corrections ΔV_{REL} must be considered to relate $\Delta\tau_\mathsf{e}$ and $\Delta\tau_\mathsf{r}$. Proper time τ and coordinate time t are related by

$$d\tau \approx \left(1 - \frac{U}{c^2} - \frac{V^2}{2c^2}\right) dt, \tag{2.4}$$

where U is the gravitational potential, V the clock velocity, and c the speed of light. Using this relation, the corrected Doppler observable is

$$N_{\mathsf{DOP}} = f_r^T \cdot \Delta\tau_\mathsf{r} - f_\mathsf{e} \cdot \Delta\tau_e + \Delta V_{\mathsf{IONO}} + \Delta V_{\mathsf{TROPO}} + \Delta V_{\mathsf{REL}}, \tag{2.5}$$

with

- $\Delta\tau_\mathsf{e}$, $\Delta\tau_\mathsf{r}$: proper time intervals of emitter and receiver between consecutive epochs

- $f_r^T = f_r^N + \Delta f_{\mathrm{r}}$: corrected receiver frequency,
- f_{e}: corrected emitter frequency,
- ΔV_{IONO}, $\Delta V_{\mathrm{TROPO}}$, ΔV_{REL}: ionospheric, tropospheric, and relativistic corrections.

Observation biases

In DORIS data processing, biases due to erroneous modeling must be estimated. Among these, a zenithal tropospheric delay is adjusted for each satellite pass to correct for inaccuracies in the modeling of the troposphere, particularly due to variations in water vapor near the beacon. Additionally, a frequency bias is estimated to account for deviations of both the transmitter and receiver frequencies from their nominal values. These frequency offsets directly affect the computed relative velocity between the satellite and the ground beacon: an error in the receiver frequency translates proportionally into a velocity error. When this frequency error remains constant during a satellite pass, it can be corrected by estimating a single frequency bias. However, if the frequency error varies over time, a frequency drift term must also be introduced, representing a linear (or higher-order) change of the frequency bias throughout the pass (J.-M. Lemoine & Capdeville, 2006).

Integrity and Performance

DORIS guarantees a 99.7% availability and a 100% signal integrity. Daily monitoring includes beacon health, transmitted power levels, broadcast coordinate checks, and validation of onboard time data. Faulty beacons are rapidly detected and excluded from processing (Jayles et al., 2006). Maintaining four to five active satellites is essential for optimal performance. Upcoming missions will extend the constellation, while parallel efforts aim to densify the beacon network, enable remote operations, and improve onboard receivers. Within the GGOS (Plag & Pearlman, 2009), DORIS remains a complementary and cost-effective technique, particularly strong in vertical positioning and long-term stability (Jayles et al., 2006).

2.2.3 Limitations

Although DORIS is a reliable geodetic technique, several limitations remain. Its performance strongly depends on maintaining at least four to five operational satellites. With fewer satellites, orbit determination and reference frame accuracy degrade significantly. In addition, despite the global beacon network, gaps remain in remote regions such as the South Pacific. Beacon failures or power outages, while rapidly detected by integrity monitoring, are still a potential source of data loss. In terms of accuracy, DORIS excels in the vertical component, making it valuable for sea-level studies, but its horizontal precision is somewhat lower compared to other space-geodetic techniques such as GNSS. Furthermore, ionospheric and tropospheric effects cannot be fully eliminated. Independent of these effects, a systematic DORIS–SLR orbit bias of about 4 cm was reported for TOPEX/Poseidon, which was traced back to an incorrect time-tagging transit time used in the ground processing (Jayles et al., 2006).

2.3 Jason-3 satellite

This chapter provides general information on the Jason-3 mission, covering its objectives, orbit characteristics, and payload.

2.3.1 Mission objectives

Jason-3 was launched in 2016 and is still operating (NASA, 2025). The Jason-3 mission is designed as a successor to the Ocean Surface Topography Mission (Jason-2) to continuously provide key satellite altimetry data for physical oceanography (Vaze et al., 2010). According to AVISO (2025b), Jason-3 was established through a cooperative agreement between four agencies, CNES, NASA, NOAA (National Oceanic and Atmospheric Administration), and EUMETSAT (European Organisation for the Exploitation of Meteorological Satellites). The Jason-3 programme is led by NOAA and EUMETSAT, with CNES acting as system coordinator and NASA supporting science team activities (AVISO, 2025b).

2.3.2 Orbit characteristics

Jason-3 operates on the same ground track used previously by TOPEX/Poseidon, Jason-1, and Jason-2, following a 254-pass, 10-day repeat orbit (NASA et al., 2020). To provide an overview of the Jason-3 orbit, only the most relevant parameters are listed in Table 1 (NASA et al., 2020).

Table 1 Key mean orbital parameters of Jason-3 (NASA et al., 2020).

Parameter	Value
Semi-major axis	7,714.432 km
Eccentricity	0.000098
Inclination	66.042°
Mean altitude (equatorial, over 1 cycle)	1,339.65 km
Repeat period	9.91564 days
Number of revolutions per cycle	127
Ground track separation (at equator)	315.55 km
Orbital speed	7.2 km/s

2.3.3 Payload

The satellite maintains the same primary instrumentation as Jason-2, including a dual-frequency radar altimeter, a microwave radiometer, and receivers of space-geodetic techniques. These are DORIS, SLR and GPS. (Vaze et al., 2010). Jason-3 has a mass of approximately 500 kg and the main payload elements include the Poseidon-3B radar altimeter supplied by CNES, NASA's Advanced Microwave Radiometer for atmospheric corrections, the DORIS positioning system also from CNES, a NASA laser retroreflector array, and a GPS receiver for complementary orbit determination (NASA et al., 2020). It utilizes signals from the GPS satellite constellation and receives dual-frequency signals from up to 12 GPS satellites, typically using about eight at a time, to achieve phase measurements with millimeter-level accuracy and pseudo-range measurements accurate to within approximately 10 centimeters (AVISO, 2025a). Jason-3 also carries two experimental instruments: the CARMEN-3 radiation detectors and the Light Particle Telescope, both of which are used to monitor the radiation environment of the on-board systems (NASA et al., 2020).

2.3.4 Mission products

The mission provides global measurements of sea surface height (SSH), significant wave height (SWH), and surface wind speed. These products are used to monitor global and regional sea level rise, study ocean circulation and its role in climate variability, and support marine meteorology, seasonal forecasting, ship routing, and coastal hazard monitoring (NASA et al., 2020).

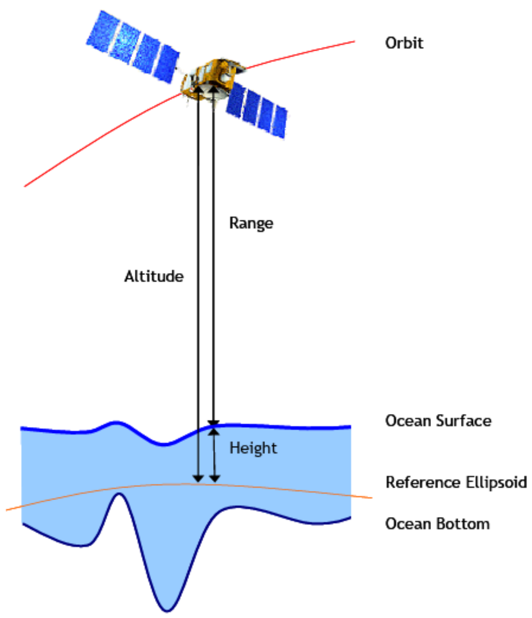

Figure 4 Functional principle of the Jason-3 satellite mission (NASA et al., 2020).

Figure 4 shows that the satellite measures sea surface height using a radar altimeter. The exact position of the satellite in orbit is necessary to derive this. Therefore, POD can be performed by using the geodetic observations, based on GPS, DORIS and SLR observations (NASA et al., 2020).

2.4 Precise orbit determination

In the following, POD is described. The principle behind it is the Gauss-Markov model, as described in chapter 2.6 with the application for combined parameter estimation in chapter 2.6.2.

2.4.1 Principle

For orbit determination, the least-squares method is used to identify the trajectory and model parameters that minimize the squared differences between observations and model predictions. Since measurements vary in accuracy and units, residuals are weighted accordingly, and the minimization applies to the weighted residuals. This approach allows trajectory and parameter estimation to be treated within a unified framework (Montenbruck & Gill, 2000).

The Kepler elements

The orbit of a satellite can be fully described using six classical orbital elements, describing an elliptical orbit (Bate et al., 1971):

- **Semi-major axis** (a): defines the size of the orbit.
- **Eccentricity** (e): describes the shape of the orbit.
- **Inclination** (i): the angle between the orbital plane and a reference plane.
- **Longitude of the ascending node** (Ω): indicates where the orbit crosses the reference plane in a northerly direction.
- **Argument of periapsis** (ω): the angle within the orbit between the ascending node and the point of closest approach (periapsis).
- **Time of periapsis passage** (T): the time at which the satellite reaches periapsis.

In DOGS-OC (DGFI orbit and geodetic parameter estimation software - orbit computation) the integration is performed using Gauss–Jackson prediction and correction (Montenbruck & Gill, 2000). Position and velocities are calculated out of the Kepler elements, which serve as start elements, resulting in the initial state vector (equation 2.6)

$$\mathbf{x}(t_0) = \begin{bmatrix} \mathbf{r}(t_0) \\ \dot{\mathbf{r}}(t_0) \end{bmatrix} = \begin{bmatrix} x(t_0) \\ y(t_0) \\ z(t_0) \\ v_x(t_0) \\ v_y(t_0) \\ v_z(t_0) \end{bmatrix}, \tag{2.6}$$

which contains the position and velocity at a reference epoch t_0. Curtis (2005) describes how the state vector can be derived from the six Kepler elements.

Equations of motion

In the idealized case where the Earth is assumed to be spherically symmetric and no perturbing forces act on the satellite, the equations of motion reduce to the classical two-body problem,

$$\ddot{\mathbf{r}} = -\frac{GM}{r^3}\mathbf{r}\,, \tag{2.7}$$

with G denoting the gravitational constant and M the Earth's mass (Beutler et al., 2003). In reality, a variety of additional forces must be considered, such as higher-order terms of the Earth's gravity field, third-body perturbations from the Moon and the Sun, and non-gravitational effects like atmospheric drag and solar radiation pressure. Accordingly, the equations of motion are extended to

$$\ddot{\mathbf{r}} = -\frac{GM}{r^3}\mathbf{r} + \delta f(t; \mathbf{r}, \dot{\mathbf{r}}, p_1, \ldots, p_m)\,, \tag{2.8}$$

where δf summarizes the perturbing accelerations and p_i with i = 1,..,m denote additional dynamical parameters to be estimated (Beutler et al., 2003).

Together with the equations of motion, the state vector defines an initial value problem whose solution yields the satellite trajectory $\mathbf{x}(t)$ (Curtis, 2005; Vallado, 2013). Using a fixed integration step, position and velocity from the state vector and acceleration from the equation of motions are propagated forward to obtain the orbit. The resulting trajectory can be represented by an osculating ellipse, described through Keplerian elements that account for perturbing influences.

2.4.2 State of the art

For Jason-3, a combined orbit solution is generated through CNES, GSFC (Goddard Space Flight Center), and NASA's JPL. These institutions independently compute precise orbits using different dynamic models and tracking techniques, including DORIS, SLR, and GNSS-based methods. They all have in common that only the model setup is published, not the parameter setup for the multi-technique POD.

Some standards define used models for POD. The POE (Precise orbit ephemeris)-F standards define the reference framework for precise orbit products of missions such as Jason-3 and Sentinel-6. They provide unified models and conventions for orbit determination, including the gravity field, tidal models and atmospheric and oceanic mass variations (Couhert et al., 2022). The POE-G standard introduces updated models and reference frames to improve precise orbit determination. DORIS and SLR station coordinates are expressed in ITRF2020 and SLRF2020 (Moyard et al., 2023). Rudenko et al. (2023) lists an overview of standards.

2.5 Orbit perturbations

Orbit perturbations describe all deviations of a satellite's trajectory from the ideal Keplerian motion. Such deviations arise from additional forces beyond the central gravitational attraction of the Earth. They can be categorized into gravitational perturbations, caused for example by the Earth's non-spherical gravity field, tides, or third-body effects, and non-gravitational perturbations, such as atmospheric drag, solar radiation pressure and relativistic effects (Montenbruck & Gill, 2000). To accurately calculate POD, the following perturbations need to be considered.

2.5.1 Gravitational perturbations

Gravitational forces from the Sun and Moon cause periodic deformations of the Earth, manifested as solid Earth tides and ocean tides, with additional contributions from pole tides. These tidal effects lead to time-variable changes in Earth's gravity field, which are commonly represented as variations in the geopotential coefficients (Combrinck, 2010; Montenbruck & Gill, 2000). The motion of a satellite is influenced by gravitational accelerations from the Sun, Moon, and planets. These third-body perturbations are typically modeled by considering the additional celestial bodies as point masses, with their contributions derived from precise ephemerides (Combrinck, 2010).

Due to general relativity, a satellite in orbit gets accelerated and cannot be neglected for POD. Therefore, a relativistic correction is needed (Combrinck, 2010). A detailed discussion of these effects, including the corresponding mathematical formulations, is provided in (Montenbruck & Gill, 2000).

2.5.2 Non-gravitational perturbations

Non-gravitational perturbations arise from forces other than gravity that act on a satellite, such as atmospheric drag and radiation pressure and are described in the following.

Atmospheric drag causes a deceleration of satellites, particularly at low altitudes. Its modeling is challenging due to uncertainties in upper atmospheric density, the complex interactions between particles and the satellite surface, and the dependence on satellite orientation relative to the particle flux. The acceleration due to drag can be approximated by

$$\ddot{\mathbf{r}}_{\text{drag}} = -\tfrac{1}{2}\, C_D\, \frac{A}{m}\, \rho\, v^2\, \mathbf{e}_v, \tag{2.9}$$

where C_D is the drag coefficient (typically 1.5 – 3.0), A the effective cross-sectional area, m the satellite mass, ρ the atmospheric density, and $\mathbf{e}_v$ the unit vector of the satellite vector v (Combrinck, 2010). For non-spherical satellites, detailed macromodels describing the geometry and optical properties of the spacecraft are provided by the IDS for DORIS satellites (International DORIS Service, 2025; Willis et al., 2016)

Solar radiation pressure results from the absorption and reflection of photons, producing an acceleration that depends on the solar flux, the satellite's effective cross-sectional area, and its mass. Assuming a simple satellite shape and that the surface normal points toward the Sun, the acceleration due to direct solar radiation pressure can be expressed as

$$\ddot{\mathbf{r}}_{\text{srp}} = -P_e \, C_R \, \frac{A}{m} \, \frac{\mathbf{r}_e}{r_e^3} \, AU^2, \tag{2.10}$$

where $P_e \approx 4.56 \times 10^{-6}$ N m^{-2} is the solar radiation flux at 1 AU, C_R is the dimensionless reflection coefficient, A the cross-sectional area, m the satellite mass, and $\mathbf{r}_e$ the geocentric position vector of the Sun. The shadow function accounts for partial or total eclipses, taking values of 0 in umbra, 1 meaning in full sunlight (Combrinck, 2010).

Earth albedo and thermal emission produce an additional radiation pressure on satellites, caused by reflection and scattering of solar radiation at the Earth's surface and atmosphere. This effect is commonly expressed through the albedo factor, with an average value of about 0.34 for Earth (Combrinck, 2010).
The resulting acceleration can be written as a sum over illuminated and visible Earth surface elements

$$\ddot{\mathbf{r}}_{\text{erp}} = \sum_{j=1}^{N} C_R \, \frac{a_j \, P_e \, A}{m} \, \cos \epsilon_j^E \, \cos \epsilon_j^S \, \frac{dA_j}{r_j^2} \, \mathbf{e}_j, \tag{2.11}$$

where C_R is the reflection coefficient, a_j the albedo factor of surface element j, P_e the solar flux at 1 AU, A/m the area-to-mass ratio of the satellite, ϵ_j^E and ϵ_j^S the incidence angles relative to the Earth and satellite surfaces, dA_j the differential Earth surface element, r_j the distance between satellite and element, and $\mathbf{e}_j$ the corresponding unit vector (Montenbruck & Gill, 2000).
Modeling this force is complicated by factors such as Earth surface orientation, atmospheric scattering, satellite surface properties, and variable cloud cover (Combrinck, 2010).

2.5.3 Other perturbations

In addition to the major perturbations, further non-gravitational forces can affect a satellite's orbit, such as the Yarkovsky thermal drag caused by temperature differences between the Earth-facing and opposite hemispheres. These effects are often difficult to model, depending on factors like the satellite's spin orientation. Moreover, small unmodelled accelerations in orbit determination are frequently accounted for through the introduction of empirical force models (Combrinck, 2010).

Summary of perturbations

The total acceleration $\ddot{\mathbf{r}}$ of a near-Earth satellite can be expressed as the sum of gravitational and non-gravitational contributions (Zeitlhöfler, 2019):

$$\ddot{\mathbf{r}} = \ddot{\mathbf{r}}_{\text{g}} + \ddot{\mathbf{r}}_{\text{ng}} = \ddot{\mathbf{r}}_{\text{kep}} + \ddot{\mathbf{r}}_{\text{ge}} + \ddot{\mathbf{r}}_{\text{3b}} + \ddot{\mathbf{r}}_{\text{rel}} + \ddot{\mathbf{r}}_{\text{drag}} + \ddot{\mathbf{r}}_{\text{srp}} + \ddot{\mathbf{r}}_{\text{erp}} + \ddot{\mathbf{r}}_{\text{other}}, \tag{2.12}$$

with

$\ddot{\mathbf{r}}_{\text{g}}$ gravitational perturbations,

$\ddot{\mathbf{r}}_{\text{ng}}$ non-gravitational perturbations,

$\ddot{\mathbf{r}}_{\text{kep}}$ undisturbed Keplerian motion,

$\ddot{\mathbf{r}}_{\text{ge}}$ gravitational acceleration due to the Earth,

$\ddot{\mathbf{r}}_{\text{3b}}$ gravitational acceleration due to third bodies,

$\ddot{\mathbf{r}}_{\text{rel}}$ relativistic accelerations,

$\ddot{\mathbf{r}}_{\text{drag}}$ acceleration due to aerodynamic drag*,

$\ddot{\mathbf{r}}_{\text{srp}}$ acceleration due to solar radiation pressure*,

$\ddot{\mathbf{r}}_{\text{erp}}$ acceleration due to Earth albedo and infrared radiation*,

$\ddot{\mathbf{r}}_{\text{other}}$ other perturbing accelerations.

Attitude-dependent perturbations are indicated with *.

2.6 Parameter estimation

In satellite geodesy, additional unknown parameters are often estimated together with the state vector (see equation 2.6 in chapter 2.4). These so-called dynamical parameters, such as coefficients for radiation pressure or atmospheric drag (Beutler et al., 2003), represent corrections to background models used for perturbing accelerations. A detailed description of these parameters is provided in chapter 2.5.
Parameter estimation in satellite geodesy is carried out within the framework of the Gauss–Markov model, which assumes unbiased observation errors with a known covariance structure (Koch, 1999). Since many geodetic observation equations are nonlinear, they are usually linearized around approximate values using a first-order Taylor expansion (Niemeier, 2008). The estimation is typically performed by minimizing the discrepancy between observed and computed values in a least-squares sense. Within the framework of the Gauss-Markov model, this approach yields the best linear unbiased estimator of the unknown parameters by minimizing a weighted quadratic form of the residuals (Koch, 1999).

According to Bloßfeld (2015) and Koch (1999), the general relationship between observations and unknowns is expressed as:

$$\mathbf{b} + \mathbf{v} = \mathbf{f}(\mathbf{x}), \tag{2.13}$$

where $\mathbf{b}$ denotes the observation vector, $\mathbf{x}$ the vector of unknown parameters, and $\mathbf{v}$ the observation errors. For nonlinear models, linearization around a priori values $\mathbf{x}_0$ leads to:

$$\mathbf{b} + \mathbf{v} = \mathbf{f}(\mathbf{x}_0) + \mathbf{A}\Delta\mathbf{x}, \tag{2.14}$$

Which results in the residual vector

$$\mathbf{v} = \mathbf{A}\Delta\mathbf{x} - \mathbf{l}. \tag{2.15}$$

In this context, the vector $\mathbf{l} = \mathbf{b} - \mathbf{f}(\mathbf{x}_0)$ represents the residuals obtained by subtracting the values computed from a priori information from the corresponding observations (Bloßfeld, 2015).

The least-squares criterion then becomes:

$$\min_{\Delta\mathbf{x}} \quad S(\Delta\mathbf{x}) = (\mathbf{A}\Delta\mathbf{x} - \mathbf{l})^\top \mathbf{P}_{ll} (\mathbf{A}\Delta\mathbf{x} - \mathbf{l}), \tag{2.16}$$

where $\mathbf{P}_{ll}$ is defined as the weighting matrix of the observations (Bloßfeld, 2015). Under the assumption of uncorrelated observations, the weighting matrix $\mathbf{P}_{ll}$ is a unit matrix and only contains elements for the main diagonal, see equation 2.27.

$$P_{ll} = \frac{1}{\sigma_i^2}, \quad P_{ll} = \begin{pmatrix} \frac{1}{\sigma_1^2} & 0 & \cdots & 0 \\ 0 & \frac{1}{\sigma_2^2} & \cdots & 0 \\ \vdots & \vdots & \ddots & \vdots \\ 0 & \cdots & 0 & \frac{1}{\sigma_n^2} \end{pmatrix} \tag{2.17}$$

Minimizing the least-squares criterion yields the normal equations:

$$\mathbf{N}\,\Delta\hat{\mathbf{x}} = \mathbf{y}, \quad \text{with} \quad \mathbf{N} = \mathbf{A}^\top \mathbf{P}_{ll} \mathbf{A}, \quad \mathbf{y} = \mathbf{A}^\top \mathbf{P}_{ll} \mathbf{l}. \tag{2.18}$$

The estimated parameter vector is then:

$$\hat{\mathbf{x}} = \mathbf{x}_0 + \Delta\hat{\mathbf{x}} = \mathbf{x}_0 + \mathbf{N}^{-1}\mathbf{y}. \tag{2.19}$$

The a posteriori variance factor is given by:

$$\hat{\sigma}_0^2 = \frac{\hat{\mathbf{v}}^\top \mathbf{P}_{ll} \hat{\mathbf{v}}}{n - u}, \tag{2.20}$$

where n is the number of observations and u the number of unknowns.
The estimated parameter vector $\hat{\mathbf{x}}$ collects all the unknown quantities that enter the observation equations and must be solved for in the adjustment process. Its exact composition depends on the measurement technique, since SLR and DORIS are sensitive to different aspects of the satellite motion, station coordinates, and measurement system. In both cases, the state vector of the satellite (position and velocity at a reference epoch) is central, but additional parameters such as station coordinates, Earth orientation parameters, and measurement biases are typically included as well (Montenbruck & Gill, 2000).

2.6.1 Combination Strategies

As discussed in Bloßfeld (2015), the combination of geodetic observations from different satellites or techniques can be realized at three hierarchical levels:

- **Observation level**: combination of original observation equations before adjustment (most rigorous, but rarely implemented across techniques);
- **Normal equation (NEQ) level**: combination of preprocessed normal equations from individual satellites or techniques (common in practice, e.g., at DGFI-TUM);
- **Solution level**: combination of independently estimated parameter solutions in a subsequent adjustment.

At DGFI-TUM, for the computation of the DTRF, the combination is primarily performed at the NEQ level using the DOGS-CS library. The combined normal equation system is constructed by summing individual NEQs, scaled by technique-specific weights and variance factors (Bloßfeld, 2015).

2.6.2 Equation system for combined paramter estimation

In this thesis, POD is based on an observation-level combination of two space-geodetic techniques, SLR and DORIS, as described below.
In the context of multi-technique orbit determination, the system of observation equations from all involved techniques forms the combined functional model. This model describes the mathematical relationship between the observations and the unknown parameters. For an individual technique, the functional model typically corresponds to Equation 2.13, which, after linearization around an initial parameter vector $\mathbf{x}_0$, leads to Equation 2.14. Bloßfeld (2015) is adopted here as the basis for the combined multi-technique model.

In a combined adjustment at the observation level, the individual functional models of all contributing techniques (here, SLR and DORIS) are unified into a single system of equations. This leads to the general relationship between observations and unknowns:

$$\begin{bmatrix} \mathbf{b}_{\text{SLR}} \\ \mathbf{b}_{\text{DORIS}} \end{bmatrix} + \begin{bmatrix} \mathbf{v}_{\text{SLR}} \\ \mathbf{v}_{\text{DORIS}} \end{bmatrix} = \begin{bmatrix} \mathbf{f}_{\text{SLR}}(x) \\ \mathbf{f}_{\text{DORIS}}(x) \end{bmatrix}, \tag{2.21}$$

where $\mathbf{b}$ denotes the observation vectors of the individual techniques, $\mathbf{v}$ the corresponding observation errors, and $\mathbf{f}(x)$ the nonlinear model functions depending on the unknown parameter vector x. Each block corresponds to one observation technique. This combined equation system constitutes the joint functional model at the observation level and forms the basis for an integrated adjustment, in which all observations contribute simultaneously to the estimation of the common parameter vector $\mathbf{x}$. The combined functional model includes the observation equations of both

SLR and DORIS. Each technique contributes its specific observable, range (ρ) for SLR and Doppler count (N_{DOP}) for DORIS, including their respective corrections. The combination is performed at the observation level, enabling a consistent and simultaneous estimation of the orbital and related parameters (Bloßfeld, 2015). Both observation equations (see Equation 2.2 for SLR and Equation 2.5 for DORIS) are nonlinear with respect to the satellite's orbital state vector $\mathbf{x}$. Therefore, they are linearized around the initial parameter vector $\mathbf{x}_0$ using a first-order Taylor expansion (see Equation 2.14). This results in the following combined linearized system:

$$\begin{bmatrix} \mathbf{b}_{\mathrm{SLR}} \\ \mathbf{b}_{\mathrm{DORIS}} \end{bmatrix} + \begin{bmatrix} \mathbf{v}_{\mathrm{SLR}} \\ \mathbf{v}_{\mathrm{DORIS}} \end{bmatrix} = \begin{bmatrix} \mathbf{f}_{\mathrm{SLR}}(\mathbf{x}_0) \\ \mathbf{f}_{\mathrm{DORIS}}(\mathbf{x}_0) \end{bmatrix} + \begin{bmatrix} \mathbf{A}_{\mathrm{SLR}} \\ \mathbf{A}_{\mathrm{DORIS}} \end{bmatrix} \Delta\mathbf{x} \tag{2.22}$$

Rewriting in residual form:

$$\begin{bmatrix} \mathbf{v}_{\mathrm{SLR}} \\ \mathbf{v}_{\mathrm{DORIS}} \end{bmatrix} = \begin{bmatrix} \mathbf{A}_{\mathrm{SLR}} \\ \mathbf{A}_{\mathrm{DORIS}} \end{bmatrix} \Delta\mathbf{x} - \begin{bmatrix} \mathbf{l}_{\mathrm{SLR}} \\ \mathbf{l}_{\mathrm{DORIS}} \end{bmatrix} \tag{2.23}$$

with

$$\mathbf{l}_{\mathrm{SLR}} = \mathbf{b}_{\mathrm{SLR}} - \mathbf{f}_{\mathrm{SLR}}(\mathbf{x}_0), \quad \mathbf{l}_{\mathrm{DORIS}} = \mathbf{b}_{\mathrm{DORIS}} - \mathbf{f}_{\mathrm{DORIS}}(\mathbf{x}_0) \tag{2.24}$$

The corresponding least-squares objective function becomes:

$$\min_{\Delta\mathbf{x}} \quad S(\Delta\mathbf{x}) = (\mathbf{A}_{\mathrm{comb}}\Delta\mathbf{x} - \mathbf{l}_{\mathrm{comb}})^\top \mathbf{P}_{\mathrm{comb}} (\mathbf{A}_{\mathrm{comb}}\Delta\mathbf{x} - \mathbf{l}_{\mathrm{comb}}) \tag{2.25}$$

where the matrices are defined as

$$\mathbf{A}_{\mathrm{comb}} = \begin{bmatrix} \mathbf{A}_{\mathrm{SLR}} \\ \mathbf{A}_{\mathrm{DORIS}} \end{bmatrix}, \quad \mathbf{l}_{\mathrm{comb}} = \begin{bmatrix} \mathbf{l}_{\mathrm{SLR}} \\ \mathbf{l}_{\mathrm{DORIS}} \end{bmatrix}, \quad \mathbf{P}_{\mathrm{comb}} = \mathrm{blockdiag}(\mathbf{P}_{\mathrm{SLR}}, \mathbf{P}_{\mathrm{DORIS}}), \tag{2.26}$$

where $\mathbf{A}_{\mathrm{comb}}$ is the combined design matrix containing the observation equations of all techniques, $\mathbf{l}_{\mathrm{comb}}$ is the combined observation (misclosure) vector, and $\mathbf{P}_{\mathrm{comb}}$ is the block-diagonal weight matrix composed of the individual technique weight matrices $\mathbf{P}_{\mathrm{SLR}}$ and $\mathbf{P}_{\mathrm{DORIS}}$. To give the different observation types a weight in combined parameter estimation, a technique-specific observation standard deviation is set in $\mathbf{P}_{\text{comb}}$. Due to the different measurement principles of DORIS and SLR (see Chapter 2.1 and 2.2), the unit for DORIS is mm/s and cm for SLR.

$$P_{\text{comb}} = \begin{pmatrix} \frac{1}{\sigma^2_{\text{SLR}_1}} & 0 & \cdots & \cdots & \cdots & \cdots & 0 \\ 0 & \frac{1}{\sigma^2_{\text{SLR}_2}} & \cdots & 0 & \cdots & \cdots & 0 \\ \vdots & \vdots & \ddots & \vdots & \vdots & \vdots & \vdots \\ 0 & 0 & \cdots & \frac{1}{\sigma^2_{\text{SLR}_n}} & 0 & \cdots & 0 \\ 0 & 0 & \cdots & 0 & \frac{1}{\sigma^2_{\text{DORIS}_1}} & 0 & \cdots \\ 0 & 0 & \cdots & 0 & 0 & \frac{1}{\sigma^2_{\text{DORIS}_2}} & \cdots \\ \vdots & \vdots & \vdots & \vdots & \vdots & \vdots & \ddots \\ 0 & 0 & \cdots & \cdots & \cdots & 0 & \frac{1}{\sigma^2_{\text{DORIS}_n}} \end{pmatrix} \tag{2.27}$$

This combined model enables the simultaneous estimation of both, common parameters (e.g., satellite orbit, station coordinates) and technique-specific parameters (e.g., frequency offsets, atmospheric delays).

2.6.3 Estimation of unknown parameters

In parameter estimation, the estimated unknowns are not only the orbit parameters as in POD (see Chapter 2.4), but also further coefficients that represent corrections to background models used for perturbing accelerations (Chapter 2.5). Following Bloßfeld (2015), the normal equations are derived from the combined functional model (Equation 2.26) as:

$$\mathbf{N_{comb}}\Delta\hat{\mathbf{x}} = \mathbf{y}, \quad \text{with} \quad \mathbf{N} = \mathbf{A_{comb}}^\top \mathbf{P_{comb}} \mathbf{A_{comb}}, \quad \mathbf{y} = \mathbf{A_{comb}}^\top \mathbf{P_{comb}} \mathbf{l_{comb}} \tag{2.28}$$

Solving this system yields the estimated corrections $\Delta\hat{\mathbf{x}}$ and the resulting parameters $\hat{\mathbf{x}}$:

$$\Delta\hat{\mathbf{x}} = \mathbf{N_{comb}}^{-1}\mathbf{y}, \quad \hat{\mathbf{x}} = \mathbf{x}_0 + \Delta\hat{\mathbf{x}} \tag{2.29}$$

The estimated residuals are given by Equation 2.30, the a posteriori variance factor is computed based on Equation 2.20.

$$\hat{\mathbf{v}} = \mathbf{A_{comb}}\Delta\hat{\mathbf{x}} - \mathbf{l_{comb}} \tag{2.30}$$

3 Single- and multi-technique POD

This chapter introduces the parameter setup used for the POD of Jason-3 based on SLR and DORIS observations. It also describes the evaluation strategy applied to assess the resulting orbit solutions using both internal and external validation criteria. The objective is to establish an optimal weighting between the two techniques, aiming to approach external orbits as closely as possible. Since no established procedures currently exist at DGFI-TUM for the setup of a multi-technique POD, this approach provides a necessary starting point. Figure 5 provides an overview of the workflow for determining and validating the optimal weighting and parameter setup for multi-technique POD.

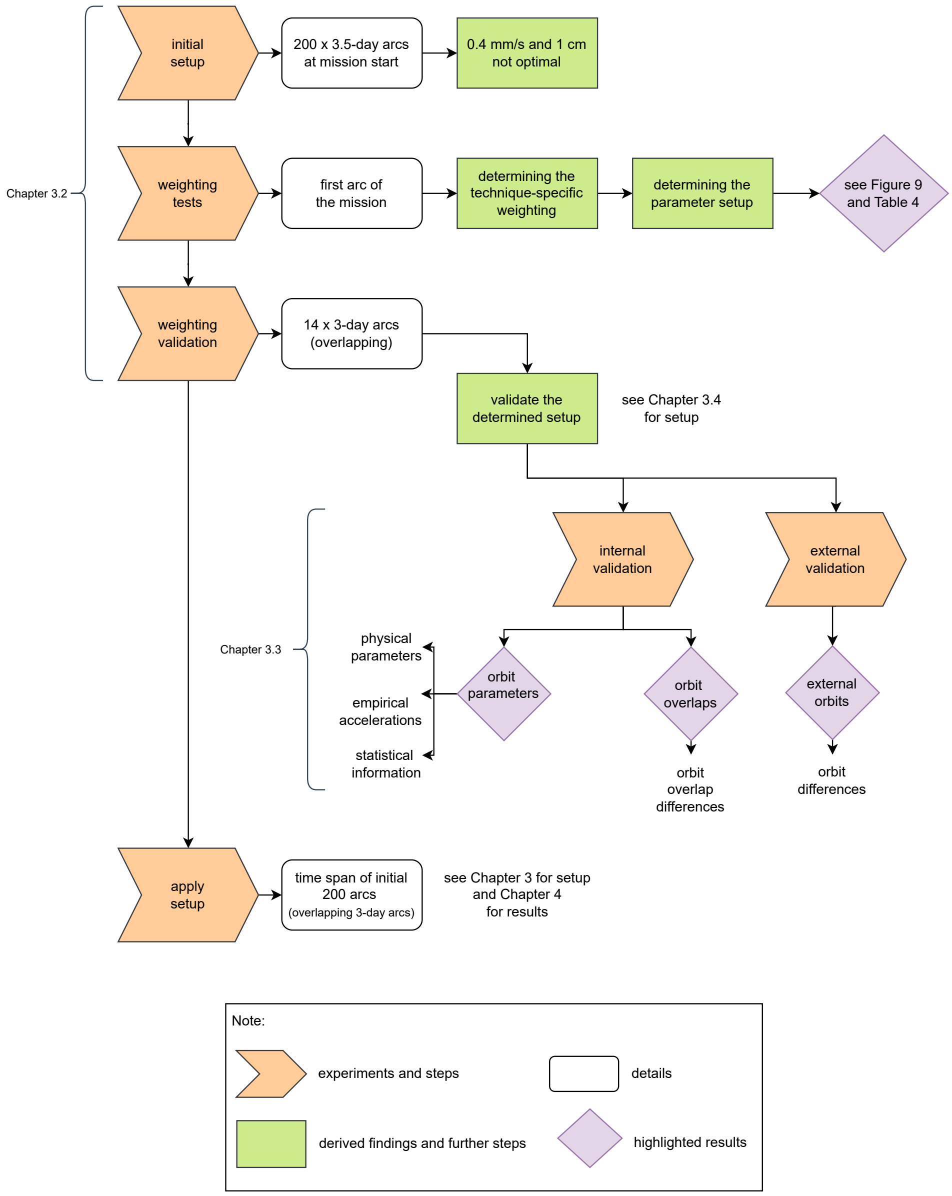

Figure 5 Workflow for determining and validating the optimal weighting setup for multi-technique POD.

3.1 POD in DOGS-OC

At DGFI-TUM, precise orbit determination is performed with the software package DOGS-OC. Developed in-house, DOGS (DGFI orbit and geodetic parameter estimation software) supports the processing of observations from different space-geodetic techniques and allows their combination within the framework of a Gauss-Markov model. The system follows a modular structure with the following main components (Bloßfeld, 2015):

- **DOGS-OC:** orbit computation,
- **DOGS-RI:** radio interferometry,
- **DOGS-CS:** combination and solution tasks.

For this study, the orbit computation and parameter estimation are carried out in DOGS-OC. The software provides different processing modes (Rudenko et al., 2024):

- **Mode 0:** Orbit integration,
- **Mode 1:** Observation simulation,
- **Mode 2:** Generation of normal equations,
- **Mode 3:** Parameter estimation.

Here, mode three is applied, corresponding to parameter estimation. For details on the available modes, see Rudenko et al. (2024).

3.1.1 General parameters

Global parameters are defined that set the overall framework for orbit determination. They specify the satellite to be processed, the reference systems and coordinate representations, the handling of observations, and the physical constants. Table 2 summarizes the basic configuration used in this work.

Table 2 General settings for multi-technique POD.

Setting	Value / Description
Satellite	Jason-3
Orbit computation options	`time=UTC, frame=CIS`
Observation options	`time=UTC, frame=TRF`
Physical constants	Earth's μ, reference radius a, J_2, speed of light c, Earth's mean rotation rate ω
Integration step size	30 s

The orbit is integrated in the Conventional Inertial System (CIS) (Rudenko et al., 2024) following the IERS Conventions (Petit & Luzum, 2010). Different output options are available and the orbit is written to the output files in the ITRF. The physical constants considered include the Earth's gravitational parameter μ, the equatorial radius a, the harmonic coefficient J_2, the speed of light c, and the Earth's mean rotation rate ω. In addition, the general settings define the estimation mode, numerical tolerances, and observation processing options. For multi-technique POD of Jason-3, both SLR and DORIS data are used, with residual thresholds of 9 cm for SLR and 3 cm for DORIS. The integration step size is 30 s, and the length of an arc for non-spherical satellites is typically 3.5 days at DGFI-TUM.

3.1.2 Perturbation Modelling

In POD, various gravitational and non-gravitational perturbations must be modeled (see Chapter 2.5). DOGS-OC applies physical background models and introduces adjustable coefficients that scale the corresponding modeled accelerations. These coefficients are estimated with predefined variances. The coefficients estimated in the orbit determination at DGFI-TUM are (Rudenko et al., 2024):

SRP (Solar radiation pressure): scales the acceleration predicted by the solar radiation pressure model to account for uncertainties in the satellite's optical properties and effective cross-sectional area (Combrinck, 2010). Estimated once per arc.

ALB (Earth Albedo): scales the acceleration caused by Earth-reflected solar radiation (albedo) and Earth-emitted infrared radiation (Combrinck, 2010). Estimated once per arc, primarily in the radial direction.

ATMO (Atmospheric drag): modifies the aerodynamic drag predicted by the atmospheric density model (Combrinck, 2010). Estimated as polygon, thus several times per arc.

EMP (Empirical Accelerations): unlike the other coefficients, this parameter is not based on a physical background model. It is an artificial coefficient introduced to absorb unmodeled effects and residual modeling errors. Empirical accelerations can be estimated in along-track, cross-track, and radial directions, typically as periodic terms once per arc and polygon sets, several times per arc.

In addition to the orbit parameters, technique-specific biases can be estimated for both SLR and DORIS observations. In the case of SLR, range biases are introduced as arc-/pass-wise offsets that account for systematic station-dependent errors, such as imperfect calibration of the timing system or uncertainties in the reference point of the retroreflector array (Combrinck, 2010). For DORIS, frequency biases are estimated to absorb residual errors in the measurement system, for instance, due to clock instabilities or antenna phase center variations (Auriol & Tourain, 2010; CNES, 2023). Also, frequency drift and scaling factors of tropospheric refraction are estimated for DORIS.
Within DOGS-OC, these biases are implemented as additional parameters in the least-squares adjustment and are estimated simultaneously with the orbital parameters, thereby reducing systematic effects in the residuals and improving the overall consistency of the combined solution (Rudenko et al., 2024).

The POD models applied in this study are consistent with those described in Rudenko et al. (2025), except for the gravity field model. Following the POE-F standards (CNES, 2018), the CNES/GRGS Earth gravity model release 04 (J.-M. Lemoine et al., 2019) is used. Although release 05 is available, release 04 was adopted to maintain consistency with external CNES orbit products. Details on these external orbits are provided in Section 3.3.3.

In this thesis, station coordinates and EOP (Earth Orientation Parameters) are not estimated but obtained from external sources. For SLR, a priori station positions and velocities are taken from SLRF2020 (version `SLRF2020_POS+VEL_2023.10.02.snx`), including periodic and post-seismic deformation corrections and using the ILRS Data Handling File (version `ILRS_Data_Handling_-File_20250206.snx`) and the ILRS eccentricity file (version `occup_ilrs_250117`) (Pavlis & Luceri, 2022). For DORIS, a priori station positions and velocities are taken from the DORIS extension of the ITRF2020 (DPOD2020 v3.1 extension), including periodic and post-seismic deformation corrections (Moreaux et al., 2023). The EOP are taken from the EOP (IERS) 20 C04 time series consistent with ITRF2020 (IERS, 2025).

3.2 Test scenarios

To combine DORIS and SLR observations for POD, suitable observation standard deviations (σ_{sys}) must be defined for each technique (see Section 2.6.2). This parameter is used in DOGS-OC to define the weighting of the different observation types (later explained in Equation 3.1 in Section 3.2.2). To derive them, a series of experiments was conducted using a subset of arcs from the mission period. An overview of the test scenarios is presented in Figure 6. The orange boxes denote the experiment steps and indicate the number of arcs used in each processing stage, while the red boxes specify the corresponding GPS weeks and the day of the week. The green boxes illustrate the subsequent processing step that follows from the current one.

As each scenario was designed to provide insights and improvements for the next, the results obtained in one configuration were systematically transferred to the subsequent processing step. In the following, these configurations are hereafter referred to as the four scenarios described in detail below. Based on this framework, the four scenarios were used to determine the technique-specific weighting between SLR and DORIS.

In the first scenario, a set of 200 arcs, each covering 3.5 days, was analyzed to obtain a general understanding of the characteristic behavior of the technique-specific systematic error standard deviation, σ_{sys}. The analyzed arcs span the period from 2016-02-17 to 2017-12-27 (arcs 18843–19813). They represent the first 200 arcs of the mission and were selected due to their high number of observations and low number of maneuvers. This investigation was intended to characterize the general orbit behavior of σ_{sys} and f_{typ}, see Equation 3.1 for details.
In this scenario, three multi-technique setups are evaluated. The σ_{sys} values are fixed to 0.4 mm/s for DORIS and 1 cm for SLR across all solutions. As shown in Equation 3.1, the three setups differ solely in their choice of f_{typ}: DGFI$_{d+s\ 1\ 1}$ adopts a value of 1 for both techniques, DGFI$_{d+s\ 1\ 2}$ as-

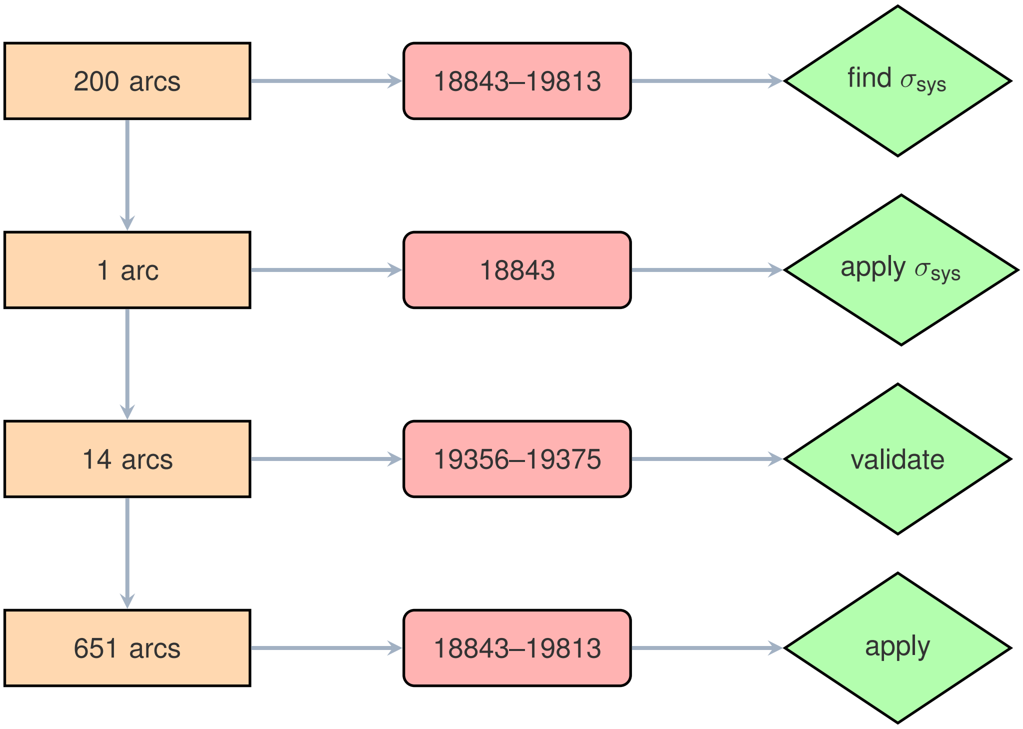

Figure 6 Test scenarios for determining the optimal σ_{sys} in multi-technique POD. Orange boxes denote experiment steps, red boxes indicate the time span in GPS weeks and the corresponding day of week, and green boxes represent outputs for subsequent processing.

signs 1 to DORIS and 2 to SLR, whereas DGFI$_{d+s\ 2\ 1}$ reverses this assignment. Taking into account both the findings of this investigation and the general weighting behavior identified in this scenario, and in view of the relationship between f_{typ} and σ_{sys}, f_{typ} is kept fixed at 1, and only σ_{sys} is varied in the subsequent scenarios.

Due to computational constraints, only the first arc of the mission (arc 18843) was processed in detail to assess suitable settings for the observation standard deviations σ_{sys} and to test different weighting strategies with respect to a reference solution.

Subsequently, 14 consecutive arcs were analyzed to validate the results obtained from the combination of the σ_{sys} values. Each arc covers a period of three days, with a one-day offset between consecutive starting epochs, spanning from 2017-02-11 to 2017-02-24 (arcs 19356–19375). The middle day of each arc is extracted for external validation. This time interval was selected because of the high number of SLR observations during the mid-mission phase, allowing for a reliable application of the derived standard deviations. Figure 7 illustrates the number of SLR observations within the 200 analyzed arcs, with the 14 selected arcs highlighted in orange.

After determining the setup for the multi-technique POD, it is applied to a longer time span, namely the time span of the initial 200 arcs at the beginning of the mission (scenario 1), to assess the resulting improvements and to enable a comparison with the reference orbits. This is shown as scenario 4 in Figure 6. For this period, consecutive 3-day arcs are generated, as this configuration showed the best performance in the analysis of the initial 14 arcs.

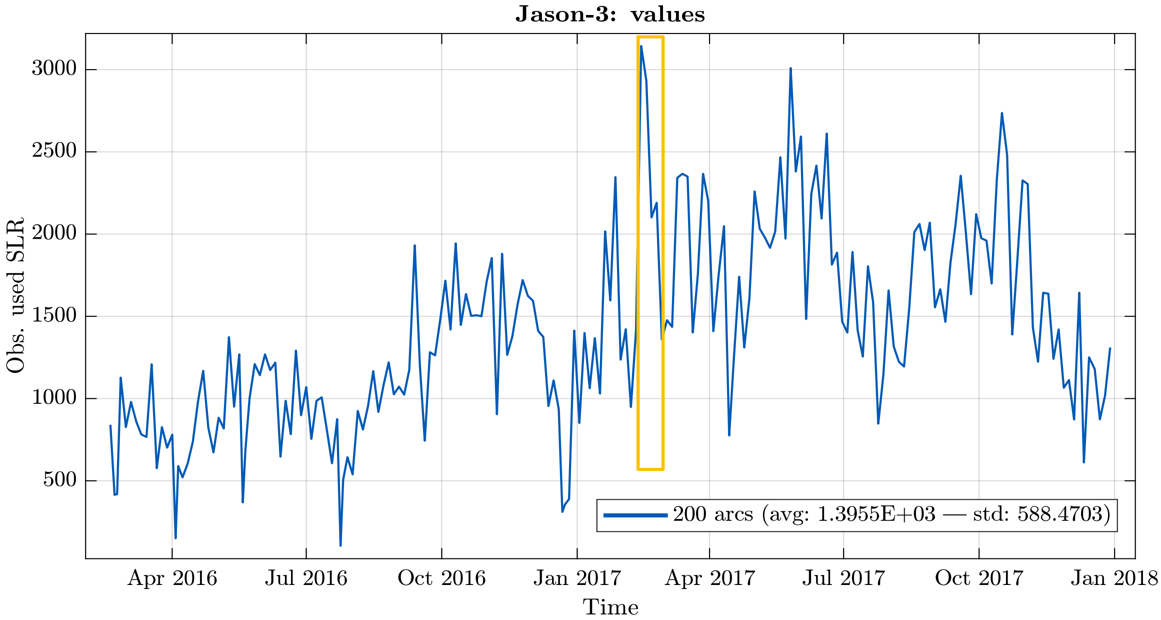

Figure 7 Number of SLR observations for 200 arcs, highlighting the chosen 14 arcs in orange.

In the first test scenario, presented as the first entry in Figure 6, the complete time span of the 200 arcs is processed using 3.5-day arcs. When a maneuver occurs within an arc, the arc is shortened, and a new arc begins immediately afterwards (Figure 8a). This represents the handling of maneuvers in DOGS-OC (Zeitlhöfler, 2019). Maneuvers were not excluded, since in the 3.5-day configuration a maneuver shortens the current arc, after which the next arc begins. The second scenario consists of a single 3.5-day arc without maneuvers, so no maneuver treatment is required. The third scenario uses the 14 arcs from the initial analysis, which lie entirely within a maneuver-free interval and therefore also require no maneuver handling.

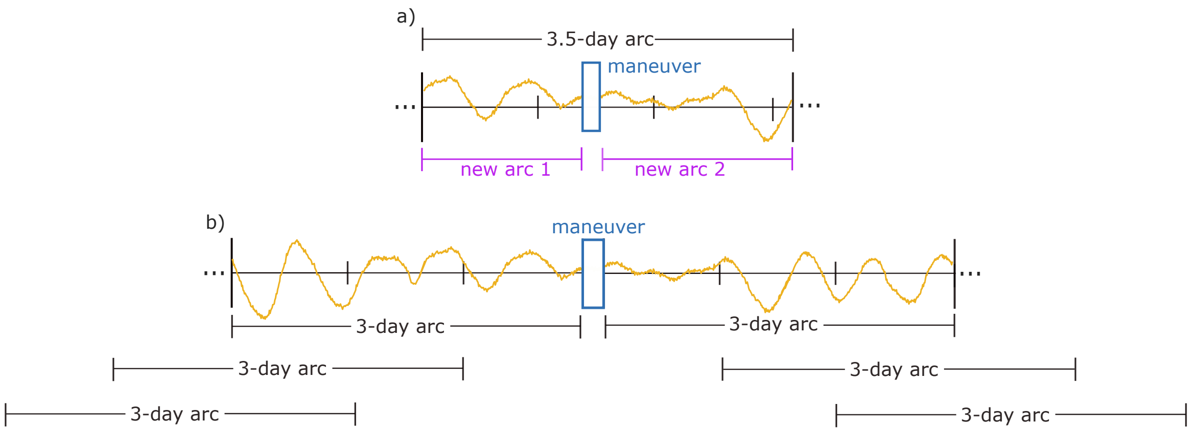

Figure 8 Handling of maneuvers in the first and last test scenario, with (a) showing the 3.5-day arc configuration (adapted from Zeitlhöfler (2019)) and (b) the 3-day consecutive overlapping arcs.

The fourth scenario covers the same time span as the first, but uses overlapping 3-day arcs. In this case, arcs are not generated when a maneuver falls within the 3-day window, since the fixed arc length would otherwise be violated and the central day could not be extracted consistently (Figure 8b). Within the 200-arc interval, nine maneuvers occur (see Table 3), each lasting approximately one minute. Maneuver epochs were identified and the affected arcs were removed from the processing where required. Table 3 lists the start and end times of all maneuvers in terms of year, month (M), day (D), hour (H), and minute (Min). For the overlapping 3-day arcs, the maneuver intervals are removed entirely, because no mid-day can be extracted when a maneuver occurs due to maneuver handling in DOGS-OC.

Table 3 Maneuvers occurring within the time span of the 200 arcs (Scenario 4).

Maneuver start						Maneuver end					
GPS week	Year	M	D	H	Min	GPS week	Year	M	D	H	Min
1885	2016	2	23	2	46	1885	2016	2	23	2	47
1891	2016	4	1	1	49	1891	2016	4	1	1	50
1897	2016	5	19	20	2	1897	2016	5	19	20	3
1907	2016	7	25	2	50	1907	2016	7	25	2	51
1914	2016	9	14	20	52	1914	2016	9	14	20	53
1928	2016	12	22	21	13	1928	2016	12	22	21	14
1944	2017	4	12	23	41	1944	2017	4	12	23	42
1965	2017	9	6	16	34	1965	2017	9	6	16	35
1979	2017	12	12	19	36	1979	2017	12	12	19	37

For the following POD determinations, the observations of 43 SLR stations and 69 DORIS beacons are used. These stations are shown in Figure 2 in Chapter 2.

3.2.1 Orbit parameter constraints

To implement the perturbation models described in Chapter 3.1.2, three scenarios were developed that differ in the choice of a priori standard deviations assigned to the orbit perturbation parameters. The objective of this setup is to identify the most suitable standard deviations derived from the external orbit comparisons (see Chapter 3.3.3 for details). Accordingly, three scenarios were defined: (1) a tc scenario (tight-constrained), (2) an lc scenario (loose-constrained), and (3) another lc scenario (loose-constrained).

In the tc (tight-constrained) scenario, all a priori standard deviations are fixed to 0.01, except for the ATMO parameters, which are constrained to 0.03. In the lc (loose-constrained) scenarios (2) and (3), these factors are generally constrained to 1.0, except for the periodic empirical accelerations (EMP), which are constrained to 2.0 $\mathrm{nm/s^2}$. Since the SRP and ALB parameters are typically well determined, both are constrained to 0.01, corresponding to tc settings. Thus, scenarios (2) and (3) are defined as lc configurations, but with SRP and ALB treated as tc. Table 4 provides an overview of the parameter setup for the three scenarios.

Table 4 Overview of the perturbation modeling scenarios and applied a priori standard deviations. N denotes the normal direction and T the transverse direction.

Parameter	(1) tc scenario	(2) lc 1 scenario	(3) lc 2 scenario
SRP [-]	0.01	0.01	0.01
ALB [-]	0.01	0.01	0.01
ATMO [-]	0.03	1.0	1.0
EMP (periodic) [nm/s²]	0.01 (NT)	2.0 (NT)	2.0 (NT)
EMP (polygon) [nm/s²]	0.01 (N)	1.0 (N)	1.0 (NT)

In scenario (1), the polygon of the empirical accelerations is only estimated in the normal direction; scenarios (2) and (3) include normal and transverse directions. For all scenarios, the periodic empirical accelerations are estimated in normal and transverse directions. For scenarios (1) and (2), the DORIS biases were estimated for all stations, and the SLR range biases were estimated per station in accordance with the ILRS Data Handling File (ILRS, 2023). In scenario (3), the SLR range biases were estimated for all stations and not according to the ILRS Data Handling File.

Scenario (3) was derived from scenario (2) during the experimental phase to achieve smaller deviations from the reference orbits. These scenarios serve as the basis for determining the optimal setup for multi-technique POD. In subsequent sections, the analysis focuses on scenarios (1) and (3) only, as scenario (2) constitutes an intermediate stage in the development of scenario (3). For simplicity, they are hereafter referred to as the tc and lc scenarios.

3.2.2 Relative weighting of DORIS and SLR

To set the weighting per technique, the optimal setup must be determined. This is performed with the first arc of the mission, which is the second step of Figure 6.

Weighting setup in DOGS-OC

In DOGS-OC, the relative weighting of each observation technique is defined as

$$W = f_{\mathrm{typ}} \cdot \frac{1}{\sigma_{\mathrm{sys}^2}}, \tag{3.1}$$

where f_{typ} represents a scaling factor used to adjust the weighting of observation types and σ_{sys} denotes the standard deviation of the systematic error component (Rudenko et al., 2024).
For each observation technique, this weighting factor W is computed individually, allowing the adjustment of the relative contribution of SLR and DORIS within the multi-technique solution.

In the subsequent experiments, f_{typ} is set to one, so that variations in the technique-specific standard deviations σ_{sys} alone determine the relative weighting between the techniques. The optimal configuration of the standard deviation for each technique must therefore be determined.

Determining the relative weighting of DORIS and SLR

As an initial configuration, σ_{sys} values of 0.4 mm/s for DORIS and 1 cm for SLR are applied, based on values established in single-technique POD analyses (personal communication, M. Bloßfeld). For a multi-technique POD, the POE-F standards specify a setup of 1.5 mm/s and 15 cm (Couhert et al., 2022). Considering the best combined POD solution for radial direction, Kong et al. (2017) use 0.2 mm/s and 15 cm for the HY-2A satellite (there called relative weights). The known standard deviation per technique for single-technique POD and the literature-based approaches for multi-technique POD serve as start values for setting the standard deviation per technique.

Figure 9 summarizes the investigated technique-specific standard deviation setups σ_{sys} and illustrates the resulting standard deviation, mean, and median differences relative to the JPL reference orbit in the radial direction. First, some tc solutions are obtained and used as input for the lc setup. Then, more variations are tested. The JPL orbit serves as a reference orbit, to which the differences are calculated and standard deviation (std. dev.), mean, and median are derived to evaluate the chosen standard deviations of multi-technique arcs. Further details on the calculation of these statistical measures are provided in Section 3.3.3. As a reference difference, the SSA orbit from CNES (see Table 6) relative to the JPL orbit is used, as it represents a realistic performance level that other orbit solutions can achieve (standard deviation: 6.9 mm, mean: 1.17 mm, median: 0.2 mm).

The results show a dependence between the relative weighting of the observations from SLR and DORIS. When σ_{SLR} is assigned a high value (i.e., a lower weight for SLR), the combined solution is dominated by DORIS, and vice versa. A systematic decrease in σ_{DOR} improves the standard deviation with respect to the reference orbit, whereas a reduction in σ_{SLR} (i.e., a higher weight for SLR) results in larger standard deviations, driving the solution toward a SLR-only orbit. In contrast, increasing σ_{SLR} shifts the solution toward a predominantly DORIS-based orbit.

Moreover, higher σ_{DOR} values are associated with increased mean offsets. In some tc scenarios, the mean and median differences show a slightly better agreement with the reference orbit compared to the lc case. Still, this improvement does not extend to the standard deviation. Consequently, the tc solutions cannot be regarded as consistent with the JPL reference orbit. Achieving a low standard deviation requires a reduction in σ_{DOR}, thereby increasing the weight of the DORIS observations. In contrast, SLR-only solutions exhibit inconsistencies with the JPL orbit.
With a stable 0.2 mm/s for DORIS and decreasing the SLR standard deviation of the systematic error part (i.e., increasing the weighting) from 100 cm to 10 cm in different steps, does not change the standard deviation of 1.15 cm. The mean decreases from -7.3 mm to -7.2 mm, with a stable median of -6.8 mm. For the values 5 mm/s to 1 mm/s, the standard deviation remains at 1.14 cm, with a mean between -7.2 mm and -8.6 mm, and a varying median between -6.7 mm and -8.3 mm. High standard deviations assigned to the systematic error component of one technique result in the combined orbit solution being effectively dominated by the other technique. For example, assigning a standard deviation of 0.2 mm/s to DORIS and 0.2 cm to SLR yields orbit differences that are nearly identical to the SLR-only solution, and vice versa.

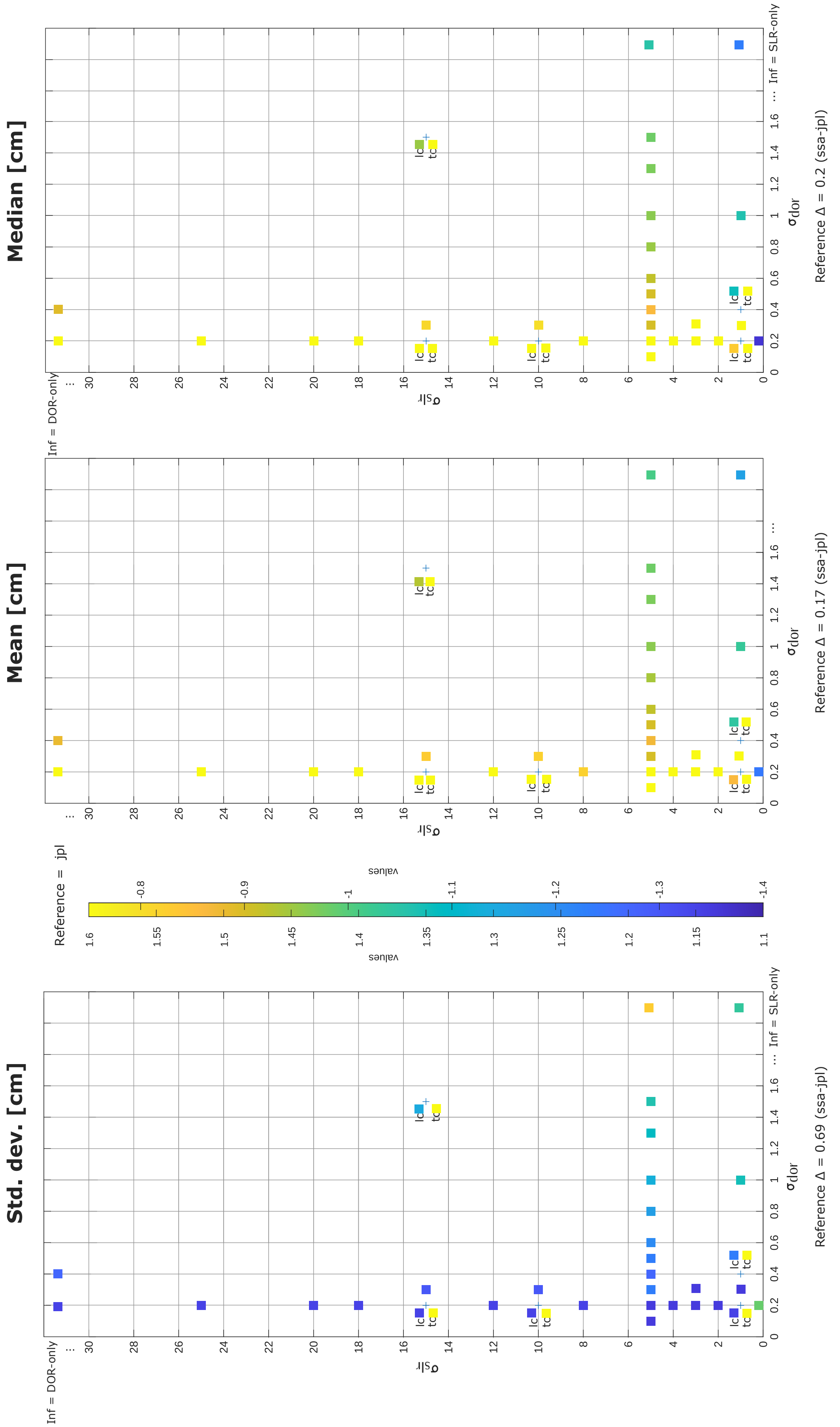

Figure 9 Technique-specific standard deviations in the context of multi-technique POD, illustrating standard deviation, mean, and median differences with respect to the JPL reference orbit in the radial component.

The best setup regarding standard deviation and mean of orbit differences in radial direction is received for standard deviation 0.1 mm/s and 5 cm with a standard deviation of 1.14 cm, mean -7.2 mm and median - 6.7 mm, showing the smallest deviation with respect to the reference difference of the SSA orbit to JPL orbit. Considering both the transverse and normal directions, 0.2 mm/s and 5 cm yield the best setup and are used as settings for the standard deviations per technique in the following.

Adjusting tc or lc setup of individual parameters

After determining the optimal technique-specific standard deviations, the individual parameters can be further adjusted by assigning them either tc or lc settings. Table 5 summarizes the tested parameter configurations for identical σ_{sys} values of 0.2 mm/s for DORIS and 5 cm for SLR. These configurations go beyond the strict tc or lc setups and include variations of the parameters described in Section 3.1.2. All listed solutions estimate range bias, frequency bias, frequency drift, and the scaling factor of tropospheric refraction. The table provides an overview of the tested parameter setups used to identify the optimal configuration. The corresponding solutions are described in detail below:

(1) All parameters are set as lc and empirical coefficients in transverse and normal direction,
(2) SRP and ALB are set as tc, all other parameters are set as lc, including empirical coefficients in transverse and normal directions,
(3) SRP and ALB are set as tc, empirical coefficients only in normal direction,
(4) SRP and ALB are set as tc plus empirical polygon in transverse and normal direction and
(5) SLR- or **(6)** DORIS-only solution with settings according to (2).

Table 5 Parameter setup testing for multi-technique POD (σ_{sys} 0.2 mm/s (DORIS) and 5 cm (SLR)) showing standard deviation, mean, and median of orbit differences with respect to the JPL orbit, with the best-performing parameter setup highlighted.

	Radial [cm]			Along-track [cm]			Cross-track [cm]		
Solution	**Std. dev.**	**Mean**	**Median**	**Std. dev.**	**Mean**	**Median**	**Std. dev.**	**Mean**	**Median**
$\text{SSA}_{\text{POE-F}}$	0.69	0.17	0.20	1.33	-0.20	-0.21	0.59	-0.03	-0.01
(1) lc aspb	1.14	-0.72	-0.67	2.91	0.35	0.30	2.53	-0.39	-0.38
(2) tcas lcpb	1.24	0.17	0.19	2.97	0.30	0.30	2.64	0.01	-0.05
(3) tcas b	1.37	0.17	0.20	3.26	0.31	0.19	2.73	0.05	-0.02
(4) tcasp b	1.36	0.17	0.20	3.26	0.31	0.19	2.73	0.05	0.00
(5) slr tcas lcpb	1.40	0.17	0.23	4.1	0.43	-0.13	4.57	0.04	0.07
(6) dor tcas lcpb	1.24	0.17	0.20	3.04	0.30	0.37	3.32	0.01	0.06

The single-technique solutions are computed to assess potential improvements achieved by the multi-technique solutions. All solutions are calculated with respect to the JPL orbit, while the reference difference is defined as the SSA orbit with respect to the JPL solution. This difference represents the deviation between two independent external orbit solutions for the same mission. It serves as a reference for evaluating the DGFI-TUM solutions, as it reflects the typical level of disagreement between established POD solutions. Solution (2) called *tcas lcpb* shows the best result for the radial direction of mean and median, and the standard deviation is only the second best. This solution is considered the best setup due to its mean and median agreement with the reference difference. Since the standard deviation setup of 0.2 mm/s (DORIS) and 5 cm (SLR), along with the parameter setup of solution (2), shows the best setting for this arc, the parameter setup is maintained for further investigations.

Furthermore, 14 mid-mission arcs were selected to validate the findings. Each arc spans three days with a one-day offset, and only the central day of each arc was analyzed to avoid boundary effects in the least-squares adjustment, where larger errors typically occur at the beginning and end.

In nonlinear least-squares orbit determination, the estimation process typically starts with relatively large residuals due to imperfect a priori information and model sensitivities. These residuals usually decrease during the iteration but may increase again if the linearization or reference trajectory becomes inadequate (Gopalarathnam, 2015). Similar divergence effects are observed in long-term orbit propagation, particularly in the radial direction and near perigee (Chen et al., 2017). Extracting only the central day of the 3-day arcs helps to minimize these effects.
The optimal standard deviations of the systematic error also apply to this time span, indicating that σ_{DOR} = 0.2 mm/s and σ_{SLR} = 5 cm yield the closest agreement with the reference solution.

3.3 Orbit validation

This section describes the methodology used to validate the DGFI-TUM orbit solutions derived from the 14-arc dataset, using both internal validation based on solution characteristics, statistical parameters, and overlap analysis, and external validation through comparisons with independent reference orbits, as illustrated in Figure 10.

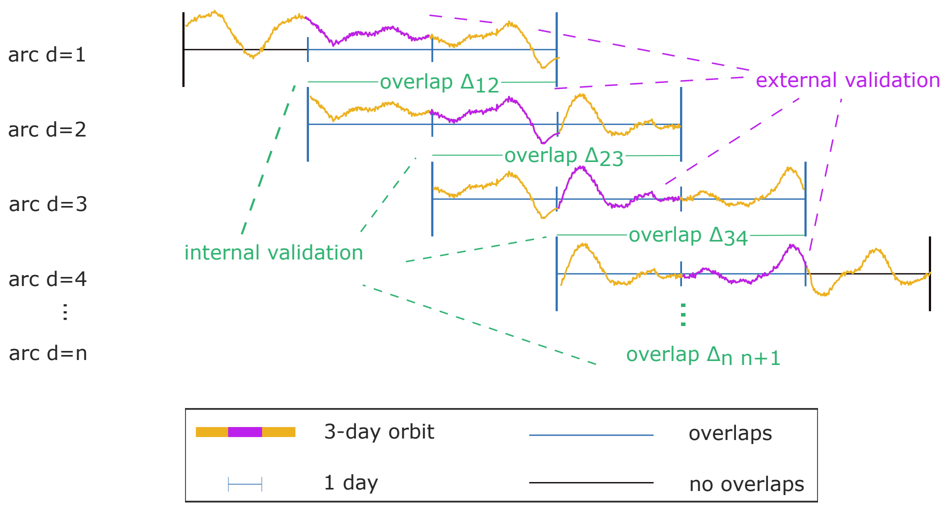

Figure 10 Internal and external orbit validation for consecutive 3-day arcs starting one day apart (start day d), showing orbit overlaps (green) and orbit differences to external orbits (purple).

3.3.1 Solution characteristics

This section describes the methodology applied to characterize the obtained orbit solutions, with a focus on convergence behavior and statistical validation metrics.

The convergence behavior and the number of iterations are obtained from the output files of DOGS-OC and used for orbit validation. Although the number of iterations is not a statistical measure, it provides qualitative information about the stability and performance of the estimation process for each arc. In principle, three different convergence behaviors can be distinguished when processing with DOGS-OC:

- **Convergence achieved**: the estimation process reaches a stable solution,
- **No convergence**: the maximum number of iterations is reached without stability,
- **Divergence**: the solution diverges instead of approaching stability.

The number of iterations indicates how reliably and efficiently the adjustment converges towards a stable solution.

Statistical parameters

According to Equation 2.15 in Chapter 2.6, the residuals $\mathbf{v}$ are the difference between the observed and the computed values. They are computed per arc per technique, and the minimum and maximum residuum are used for the validation of the solution.

In classical geodetic adjustment theory, the mean square error is defined as the positive and negative square root of the variance and therefore corresponds to the standard deviation (Koch, 1999; Niemeier, 2008). It expresses the dispersion of a random variable about its expected value. In contrast, the RMS value, as implemented in MATLAB, is computed as

$$x_{\mathrm{RMS}} = \sqrt{\frac{1}{N}\sum_{n=1}^{N}|x_n|^2}, \tag{3.2}$$

where N is the number of samples and x_n are the individual observations (MathWorks, Inc., 2025). Unlike the standard deviation, the RMS is calculated without subtracting the mean and therefore represents the quadratic mean of the values themselves. In this analysis, the RMS is computed for each arc and technique.

3.3.2 Orbit parameter validation: internal validation

For internal validation, both physical and empirical parameters relevant to force modeling, as discussed in Chapter 3.1.2, must be taken into account. Among the physical parameters, the solar radiation pressure coefficient, the Earth's albedo coefficient, and the atmospheric drag coefficient are considered. These parameters primarily serve as scaling factors of the force models and should generally remain within a range close to one.

In addition to the physical parameters, the empirical accelerations must be analyzed, as they serve to compensate for deficiencies in the force models, including unmodeled or inaccurately modeled effects. The magnitude and variability of these accelerations indicate how well the physical effects influencing satellite motion are modeled. Large empirical accelerations indicate significant modeling errors or unknown disturbing forces. Empirical accelerations are generally divided into two types: periodic and as polygon constant. Both types include components in the radial, normal, and transverse directions. Ideally, when the physical models fully capture the orbital dynamics, these empirical accelerations should approach zero. This suggests that the empirical terms do not account for a significant amount of unmodeled effects.

Orbit overlap differences

As a second component, internal validation of the derived orbit solution can be performed using overlapping orbit arcs. With a temporal overlap of two days between consecutive arcs, position differences at common epochs can be computed. This enables an assessment of the consistency between successive orbit segments and provides a measure of the internal quality and stability of the orbit determination. In this study, 14 consecutive 3-day arcs are computed. The overlap between two successive arcs, corresponding to the common time span, is then determined. The following section provides details about the statistical analysis of orbit overlaps.

To evaluate the orbit overlap differences, the mean, standard deviation, and maximum difference between the overlaps are calculated.
The arithmetic mean $\bar{x}$ represents the most common estimator for the central value of a set of observations and is calculated as

$$\bar{x} = \frac{1}{n}\sum_{i=1}^{n} l_i \qquad \Rightarrow \qquad \bar{d} = \frac{1}{n}\sum_{i=1}^{n} d_i, \tag{3.3}$$

where l_i denotes the individual observations and n is the total number of observations (Niemeier, 2008). The right formulation is the adaptation used to validate the orbit overlap differences, where d_i denotes the individual differences between two corresponding values.

Following Niemeier (2008), the standard deviation, as the square root of the empirical variance, is defined as

$$s_0 = \sqrt{\frac{1}{n}\sum_{i=1}^{n} \varepsilon_i^2} \qquad \Rightarrow \qquad s_d = \sqrt{\frac{1}{n}\sum_{i=1}^{n} d_i^2}, \tag{3.4}$$

where n is the number of observations, ε_i denotes the individual residuals (differences between the observed and the estimated values). The right formulation is used for the overlap differences, where d_i represents the individual orbit overlap differences between two corresponding values.

In addition to the statistical parameters described above, the maximum values of the differences were also determined to quantify the range of the deviations between the arcs. This value provides information about the largest discrepancies between the compared datasets.

3.3.3 Orbit parameter validation: external validation

To validate the derived multi-technique orbit solution, it is essential to perform a comparative analysis against independent external orbit products. The reference solutions available from JPL, CNES, and GSFC are listed in Table 6.

Table 6 External single- and multi-technique orbits.

Solution	Institute	Technique(s)	Source
JPL_{poe}	JPL	GPS	JPL (2020) and Desai et al. (2020)
$\text{SSA}_{\text{POE-F}}$	CNES	DORIS and GPS	CDDIS (2020)
$\text{GSFC}_{\text{std2400}}$	GSFC	DORIS and SLR	F. G. Lemoine et al. (2025)

In this context, the CNES POE-F orbit product appears under the name SSA, as the CNES Associate Analysis Center (AAC) is listed under this name within the IDS Data Centers (F. Lemoine & Moreaux, 2021). The orbit is therefore referred to as the SSA orbit in this work.
Two approaches can be used for the validation. In the first approach, the orbit arcs are calculated without any temporal overlap, meaning they follow one after the other in time. In the second approach, the arcs overlap in time, and the middle day of each arc is used for validation to overcome the least-squares problem named in Chapter 3.2. This approach is used to validate the derived solution.

Statistical analysis of orbit differences

To evaluate the quality of the determined orbits, differences with respect to the external orbits are analyzed using standard statistical measures. For the 14 selected arcs, the reference orbits (Table 6) are considered to obtain the best alignment of the DGFI-TUM solution.
For each arc, the radial, along-track, and cross-track orbit differences Δx_i are computed relative to the reference orbit, from which the mean, median, and standard deviation are derived.

The arithmetic mean $\bar{x}$ is also used to evaluate the orbit differences to the external orbit. It is calculated using the formula 3.3 from the orbit overlap differences, where d_i now denotes the orbit overlap differences between two corresponding values.

Following Niemeier (2008), the median x_m represents the middle value of an ordered set of observations. For its computation, the observations l_i are first arranged in ascending order

$$l_{(1)} \leq l_{(2)} \leq \cdots \leq l_{(n)}, \tag{3.5}$$

forming the ordered vector. The median is then obtained as the central value of an ordered sample, corresponding to the middle observation for odd n or the mean of the two central observations for even n.

$$x_m = \begin{cases} l_{\left(\frac{n+1}{2}\right)}, & \text{for odd } n, \\ \frac{1}{2}\left(l_{\left(\frac{n}{2}\right)} + l_{\left(\frac{n}{2}+1\right)}\right), & \text{for even } n, \end{cases} \tag{3.6}$$

where n denotes the total number of observations. For the differences between two orbits, the median of the differences d_m is obtained by ordering the orbit differences in equation 3.5 and replacing the observations l_i with the ordered differences d_i.

The standard deviation of orbit differences is calculated by equation 3.4, where now d_i represents the individual orbit differences between two orbit solutions.

3.4 Derived settings for multi-technique POD

After the determination of the best values for the standard deviation of the systematic error for the multi-technique POD and the setup for the parameter constraints, the derived settings for multi-technique POD using DORIS and SLR observations are described in Table 7. As described in Section 3.2.2, the standard deviation of the systematic error part is set to 0.2 mm/s for DORIS and 5 cm for SLR. The estimated parameters are set up according to the lc-scenario from Section 3.2.

Table 7 Setup of technique-specific standard deviations, a priori standard deviations, and estimated biases for multi-technique POD.

Parameter / Bias	**Setup**
σ_{DORIS}	0.2 mm/s
σ_{SLR}	5 cm
SRP	0.01
ALB	0.01
ATM	1.0
EMP$_{\mathrm{periodic}}$ (1/rev, N+T direction)	2.0 $\mathrm{nm/s^2}$
EMP$_{\mathrm{polygon}}$ (12h, N+T direction)	1.0 $\mathrm{nm/s^2}$
Frequency bias	per station, per pass
Frequency drift	per station, per arc
Scaling factor of tropospheric refraction	per station, per pass
Range bias	per station, per pass
Time bias	not estimated

Scaling factor of tropospheric refraction, frequency bias, and range bias are estimated for all stations per pass. The frequency drift is estimated per station once per arc. For Jason-3, the DORIS system time biases, also called time tag, are only on the order of 1 - 2 µs, compared to up to 10 - 20 µs in earlier missions such as TOPEX/Poseidon and Envisat (F. G. Lemoine et al., 2018). Three biases are already estimated for DORIS: frequency drift, frequency bias, and scaling of tropospheric refraction. The DOGS-OC software at DGFI-TUM is currently not capable of estimating additional DORIS-specific biases. Adjusting this bias solely for SLR would degrade the performance of the DORIS solution (personal communication, M. Bloßfeld). Therefore, and considering its comparatively small magnitude reported in the literature, this bias is not estimated in the present analysis.

4 Results and discussion

To assess the quality of the derived multi-technique solutions, an orbit validation was performed, which comprises both internal and external validation. The internal validation involves the analysis of estimated physical parameters and biases, statistical metrics, as well as orbit overlap differences, whereas the external validation is based on orbit differences with respect to reference orbits from JPL and SSA.

In Chapter 3.2.2, the optimal σ_{sys} values were determined as 0.2 mm/s for DORIS and 5 cm for SLR, when considering all three directions and referred to as solution d+s 0.2 5 in Figure 11. When only the radial direction is taken into account, 0.1 mm/s for DORIS and 5 cm for SLR show the best setup for the technique-specific standard deviations, denoted as solution d+s 0.1 5. In Figure 11 the respective single-technique solutions are called SLR-only 5, DORIS-only 0.2 and DORIS-only 0.1. These values were derived from the single-arc experiment and confirmed by the 14-arc analysis. Because these two weighting setups were confirmed as the best two solutions, the corresponding results are presented for the 14 arcs below. For visual clarity, the different solutions are highlighted in blue.

4.1 Internal validation

The findings of the aforementioned parameters are summarized in Figure 11. It is essential to note that these values represent the entire 3-day arcs rather than only the central day, which is extracted for external validation. The parameters remain valid, since ALB and SRP parameters are estimated once per arc and are therefore representative of the entire interval, as they are influenced by all observations. In contrast, the empirical accelerations are estimated multiple times within each arc at different epochs. These provide additional information for validating the single-day segment of the 3-day arcs.

4.1.1 Physical parameters

Figure 11a presents the average values of the physical parameters and the estimated biases, which will be addressed in the following subsection. The physical parameters comprise ALB, SRP, and ATMO. In addition, unmodeled physical effects are absorbed by EMP parameters, providing an indication of how well the orbit dynamics are represented by the applied force models. The black polygon, representing reference values in Figure 11a, indicates the ideal values that the parameters and coefficients would take in a perfectly physically determined solution. There, the physical parameters, as scaling factors, should be close to one, whereas the empirical accelerations should be as close to zero as possible and are expressed in nm/s^2.

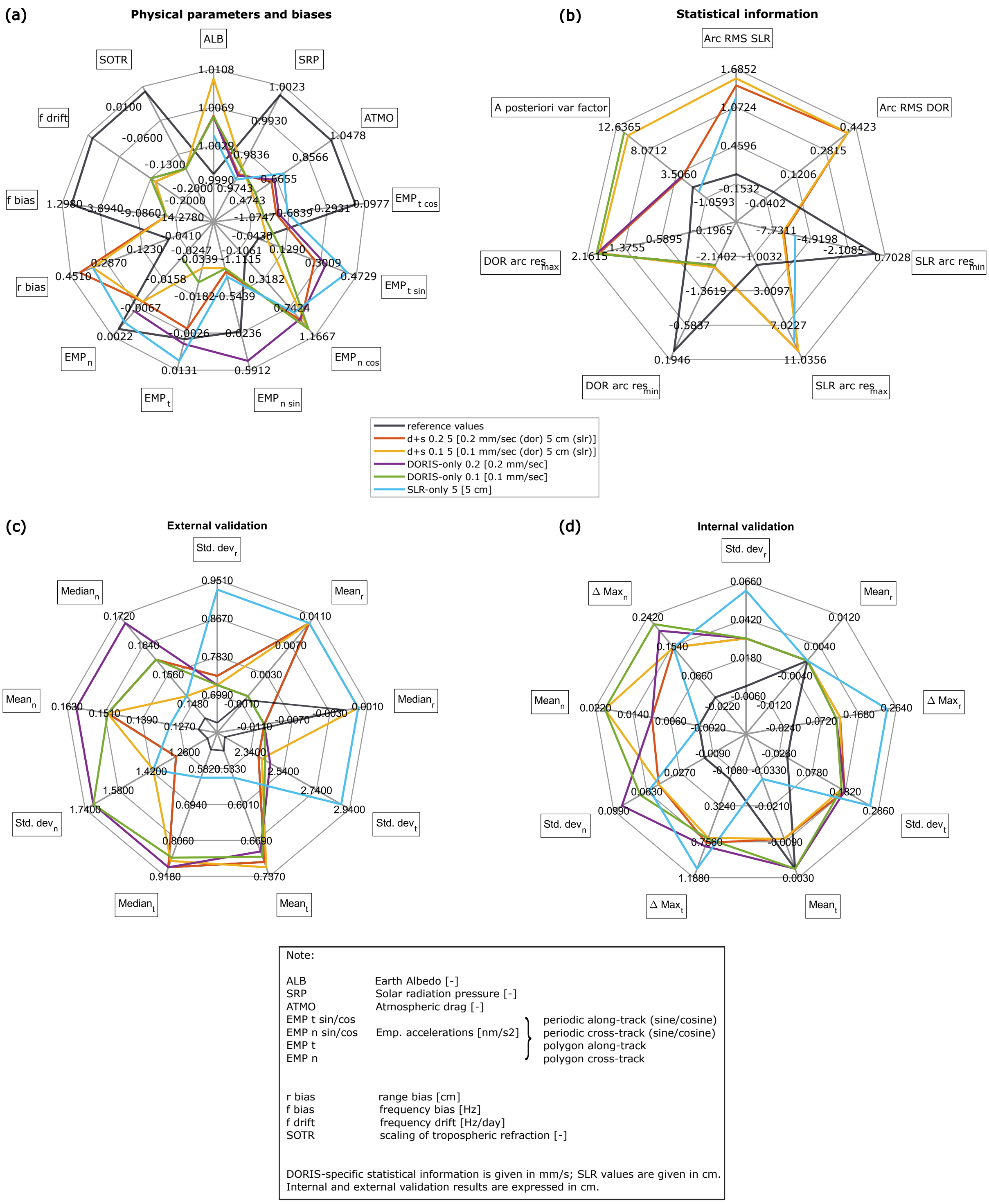

Figure 11 Average values of physical and statistical parameters of the best multi-technique DGFI-TUM solutions, shown in comparison with the respective single-technique solutions, including internal and external validation (with respect to the SSA orbit).

The combined solutions d+s 0.2 5 and d+s 0.1 5 exhibit similar values for both the physical parameters and the empirical accelerations. The average earth albedo coefficient (ALB) $\pm$ standard deviation amounts to 1.0060 $\pm$ 0.0024 for d+s 0.2 5 and 1.0098 $\pm$ 0.0065 for d+s 0.1 5. The atmospheric drag coefficient (ATMO) and the sine component of the periodic transverse accelerations (EMP t_{sin}) are smaller for d+s 0.1 5 (ATMO 0.5221 $\pm$ 1.2191 and EMP t_{sin} 0.0497 $\mathrm{nm/s^2}$ $\pm$ 1.0940) than for d+s 0.2 5 (ATMO 0.6357 $\pm$ 0.5346 and EMP t_{sin} 0.2729 $\mathrm{nm/s^2}$ $\pm$ 0.4567), whereas the opposite is observed for the remaining parameters. The slightly smaller ATMO coefficient in the d+s 0.1 5 solution indicates a reduced atmospheric drag compensation, showing slightly larger periodic empirical corrections in the transverse and normal directions. Overall, the two combined solutions show only minor differences.

The single-technique solutions DORIS-only 0.2 and DORIS-only 0.1 show minor differences in physical parameters, as well as small deviations from the combined solutions. This confirms that the combination does not notably distort the individual technique characteristics. The empirical accelerations are slightly smaller for the DORIS single-technique solutions (ranging from -0.8500 $\mathrm{nm/s^2}$ $\pm$ 0.4493 to 0.9152 $\mathrm{nm/s^2}$ $\pm$ 0.3240), whereas ranging from -0.9147 $\mathrm{nm/s^2}$ $\pm$ 0.4528 to 0.9375 $\mathrm{nm/s^2}$ $\pm$ 0.2372 for d+s 0.2 5 and -0.9770 $\mathrm{nm/s^2}$ $\pm$ 0.6294 to 1.0553 $\mathrm{nm/s^2}$ $\pm$ 0.3909 for d+s 0.1 5. The maximum deviation between the two DORIS-only solutions amounts to 0.2 $\mathrm{nm/s^2}$, showing marginal differences.

The SLR-only 5 solution exhibits comparable physical parameters and empirical accelerations. The amplitudes of the EMP are generally smaller (-0.7035 $\mathrm{nm/s^2}$ $\pm$ 0.2509 to 0.8157 $\mathrm{nm/s^2}$ $\pm$ 0.1750), and the reduced variability of the EMP parameters in the SLR-only 5 solution indicates a more stable behavior.

4.1.2 Biases

The average values per solution are shown in Figure 11a and summarized in Table 8. They represent the mean of the technique-specific biases, showing SLR range bias (R bias), DORIS frequency bias (F bias), frequency drift (F drift), and scaling factor of tropospheric refraction (SOTR). According to the numbers, the mean SLR range bias for the d+s 0.1 5 configuration is smaller and closer to the SLR-only solution compared to d+s 0.2 5. These values were computed to be included in Figure 11a, but they cannot be interpreted as a general indicator of systematic differences between the solutions, as they are mean values per solution, not considering individual station behavior.

Table 8 Mean values of estimated biases for each combined solution (d+s 0.2 5 and d+s 0.1 5) and their corresponding single-technique solutions.

Solution	R bias [cm]	F bias [Hz]	F drift [Hz/day]	SOTR [-]
DGFI$_{d+s\ 0.2\ 5}$	0.41	-12.98	-0.14	-0.16
DGFI$_{d+s\ 0.1\ 5}$	0.35	-12.98	-0.14	-0.16
DGFI$_{DORIS-only\ 0.2}$		-12.98	-0.13	-0.16
DGFI$_{DORIS-only\ 0.1}$		-12.98	-0.13	-0.16
DGFI$_{SLR-only\ 5}$	0.35			

To classify the bias values, Figure 12 illustrates the differences in biases between the combined solution and the respective single-technique solution. The blue bars represent the differences between the d+s 0.2 5 solution and the respective single-technique solutions. In comparison, the orange bars correspond to the differences between the d+s 0.1 5 solution and the respective single-technique solutions. The stations are sorted in descending order according to the number of observations.

During the time span covered by the 14 analyzed arcs, observations from 50 DORIS and 30 SLR stations were used. Accordingly, Figure 12 shows this number of estimated biases.

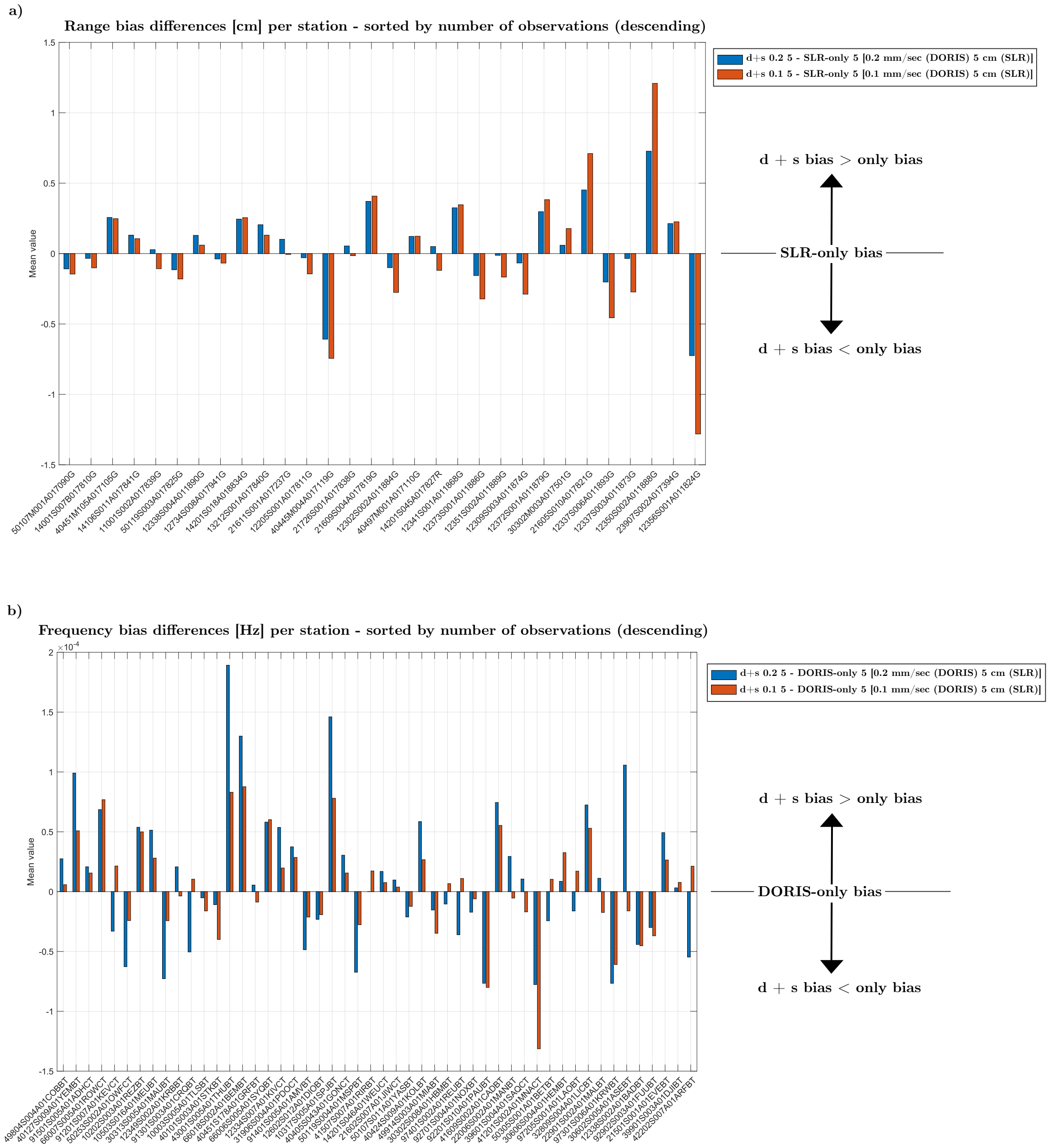

Figure 12 Frequency bias [Hz] and range bias [cm] differences per station, sorted by number of observations (descending).

In Figure 12a, representing the range bias differences, it can be observed that for most stations the orange bars are larger than the blue ones. This indicates that the difference between the d+s 0.1 5 solution and its corresponding single-technique solution is larger than that between the d+s 0.2 5 combination and its respective single-technique solution. The underlying reason is that the standard deviation of the DORIS component in the combined d+s 0.2 5 solution is larger, which reduces its relative weight in the combination. As a result, the combined solution tends to be closer to the SLR-only solution. In general, the larger the DORIS standard deviation becomes, the more the solution shifts toward an SLR-only solution, resulting in a smaller difference to the SLR range biases. Overall, a general trend can be observed for the analyzed period: stations with a higher number of available observations tend to exhibit smaller range biases and smaller bias differences.

The second plot, Figure 12b, illustrating the frequency bias differences, shows a general tendency for the blue bars to be larger than the orange ones. The blue bars represent the differences between the d+s 0.2 5 solution and the respective single-technique solutions. In comparison, the orange bars correspond to the differences between the d+s 0.1 5 solution and its respective single-technique counterparts. Since the d+s 0.2 5 solution is associated with a larger DORIS standard deviation, the relative weight of the DORIS observations is smaller. Conversely, the multi-technique d+s 0.1 5 solution has a smaller standard deviation, resulting in a higher weighting of DORIS. Consequently, the combined d+s 0.1 5 solution tends to be closer to the DORIS-only solution, which explains why the corresponding orange bars are smaller.

Additionally, the frequency drift and the scaling factor of the tropospheric refraction were analyzed and plotted in the same manner, i.e., sorted by station and number of observations. Since no consistent or systematic behavior could be identified, these results are not shown here.

4.1.3 Statistical information

Figure 11b shows the statistical information about the derived multi-technique solutions with the respective single-technique solutions.

The combined solutions d+s 0.2 5 and d+s 0.1 5 exhibit very similar residual characteristics for both techniques, with only minor differences in the RMS of the residuals, using the same number of observations. For the arc RMS of SLR, the RMS increases slightly from 1.42 cm $\pm$ 0.1248 cm (for d+s 0.2 5) to 1.53 cm $\pm$ 0.1212 (for d+s 0.1 5), while the arc RMS of DORIS remains constant at 0.40 mm/s ($\pm$ 0.0029 mm/s for d+s 0.2 5, $\pm$ 0.0027 mm/s for d+s 0.1 5. The arc residual ranges (minimum and maximum residuals) are nearly identical for both techniques and setups, ranging from a minimum value of -6.9 cm $\pm$ 3 cm to a maximum value of 10.1 cm $\pm$ 3 cm, indicating a consistent overall fit to the observations and confirming the general stability of the combined adjustment.

For the single-technique solutions, the residual magnitudes are of the same order. The DORIS-only 0.2 and DORIS-only 0.1 solutions yield almost identical RMS values (0.4021 mm/s vs. 0.4020 mm/s $\pm$ 0.0026), demonstrating the internal consistency of the DORIS processing. The SLR-only 5 solution shows slightly smaller arc RMS SLR values (RMS = 1.23 cm $\pm$ 0.1379) compared to the combined cases, which is expected since no relative weighting between different observation techniques is required.

A more distinct difference appears in the a posteriori variance factors, which increase from 2.73 $\pm$ 0.0670 (solution d+s 0.2 5) to 10.90 $\pm$ 0.2607 (solution d+s 0.1 5). This indicates that the d+s 0.1

5 configuration leads to a less consistent stochastic behavior, suggesting an imbalance between the two techniques. The single-technique solutions show similar behavior. Their a posteriori variance factors differ significantly, with values of 2.88 $\pm$ 0.0397 for DORIS-only 0.2, 11.50 $\pm$ 0.1570 for DORIS-only 0.1, and 0.08 $\pm$ 0.0240 for SLR-only 5.

These results confirm that the d+s 0.1 5 setup tends to overweight DORIS, while the SLR-only 5 solution remains internally very stable but underestimates the overall variance level due to the smaller number of observations. Consequently, the d+s 0.2 5 configuration provides the most balanced weighting between both techniques and results in the most consistent combined solution. The a posteriori variance factor of 2.73 $\pm$ 0.0670 for the d+s 0.2 5 solution represents a consistent result, given the a priori value of 1.0. It indicates that the actual standard deviation is about 1.6 times larger than assumed (corresponding to $\sqrt{2.73}$), but still within a realistic range. The factor reflects the overall adjustment quality and depends on all estimated parameters, not solely on the applied weighting factors.

When aiming to bring the a posteriori variance factor of the combined solution close to 1, the solution d+s 0.35 1 provides the closest values, yielding 0.9027 $\pm$ 0.2060.

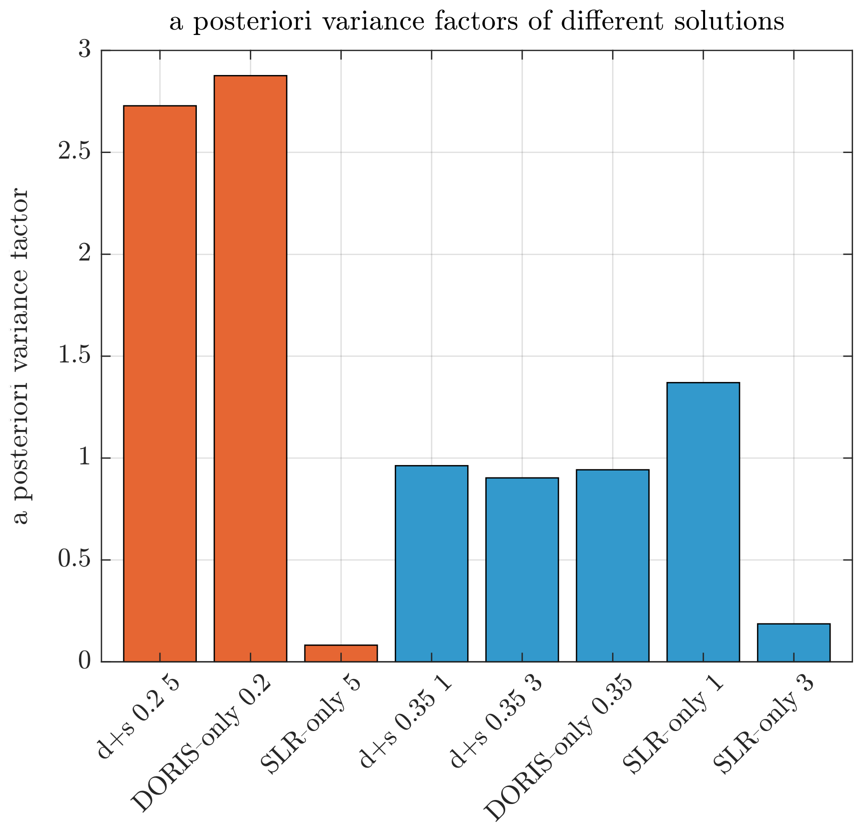

Figure 13 Comparison of a posteriori variance factors between multi-technique and corresponding single-technique solutions.

For DORIS-only 0.35, this corresponds to 0.9424 $\pm$ 0.0127, while for SLR-only 1 it results in 1.3701 $\pm$ 0.2341. The d+s 0.35 3 solution also performs well (0.9625 $\pm$ 0.0152). However, the single-technique solution SLR only 3 deviates significantly from the target value, with an a posteriori variance factor of 0.1865 $\pm$ 0.0431. This is caused by applying the multi-technique σ_{sys} to a single-technique solution. The SLR only 1 solution using a σ_{sys} of 1 cm yields a value much closer to one, which is also the recommended single-technique configuration described in Section 3.2.2.

Figure 13 shows the a posteriori variance factors of different solutions. The orange bars denote the solution that best matches the SSA orbit (d+s 0.2 5) and the respective single-technique solutions, whereas the blue bars correspond to combined solutions with variance factors closest to one. The solution d+s 0.35 3 exhibits larger deviations from the external orbits, and therefore is not regarded as the optimal setup (Table 10 in Section 4.2). The physical parameters and biases listed in Section 4.1.1 and 4.1.2 are of a similar magnitude to those obtained in the d+s 0.2 5 solution.

In summary, all configurations exhibit consistent parameter behavior, demonstrating the robustness of the estimation process due to the overall consistency of the different solutions. The combined solutions benefit from both the stability of SLR and the sensitivity of DORIS, resulting in balanced physical coefficients and moderate empirical accelerations.

4.1.4 Orbit overlaps

Figure 11d shows the orbit overlap differences within each solution, including both multi- and single-technique solutions. Per direction, the mean, standard deviation, and Δ max are calculated. In the ideal case, all these values are zero, i.e., there are no differences between subsequent arcs. The black reference values mark this.

Table 9 Statistical comparison of orbit overlaps for different DGFI solutions (d+s 0.2 5 and d+s 0.1 5) with their corresponding single-technique solutions, including the mean, standard deviation, and maximum absolute differences per direction (cm).

	Radial [cm]			Transverse [cm]			Normal [cm]		
Solution	**Std. dev.**	**Mean**	$\Delta_{\max}$	**Std. dev.**	**Mean**	$\Delta_{\max}$	**Std. dev.**	**Mean**	$\Delta_{\max}$
DGFI$_{d+s\ 0.2\ 5}$	0.03	0.00	0.12	0.18	-0.01	0.77	0.05	0.01	0.15
DGFI$_{d+s\ 0.1\ 5}$	0.03	0.00	0.12	0.17	-0.01	0.71	0.05	0.02	0.15
DGFI$_{SLR-only\ 5}$	0.06	0.00	0.24	0.26	-0.03	1.08	0.06	0.00	0.15
DGFI$_{DORIS-only\ 0.1}$	0.03	0.00	0.11	0.17	0.00	0.72	0.07	0.02	0.22
DGFI$_{DORIS\ only\ 0.2}$	0.03	0.00	0.11	0.18	0.00	0.81	0.09	0.01	0.20

Table 9 summarizes the statistical metrics of the orbit overlap differences for the radial, transverse, and normal directions, showing the combined solutions and the respective single-technique solutions. For each solution, the standard deviation (std. dev.), mean, and maximum absolute difference are provided.

The radial differences exhibit the smallest overall variations. Both combined DGFI-TUM solutions show a standard deviation of 0.03 cm, which is identical to the DORIS-only solutions. In contrast, the SLR-only solution reveals a larger scattering (std. dev. = 0.06 cm). The maximum differences range between 0.11 and 0.12 cm for the combined and DORIS-only solutions, while the SLR-only solution reaches 0.24 cm. The mean radial difference of 0.00 cm indicates that no systematic bias is present in the radial direction. The choice between the two combined solutions (d+s 0.2 5 vs. d+s 0.1 5) does not affect the orbit overlap differences in radial direction.

The transverse direction shows larger deviations: The combined solutions achieve standard deviations of 0.17 cm and 0.18 cm, which are slightly better than the DORIS-only values and noticeably better than the SLR-only values (0.26 cm). The maximum differences are highest for the SLR-only solution (1.08 cm), while the combined solutions are significantly lower (0.71 cm and 0.77 cm). The transverse component benefits from the combined approach. The combination reduces both the overall spread and the maximum outliers compared with the single-technique solutions. Differences between the two combined weighting schemes remain negligible.

In the normal direction, the combined solutions again show the most stable behavior. Both combined setups yield a standard deviation of 0.05 cm, which is lower than the DORIS-only solutions (0.07 cm vs. 0.09 cm) and slightly lower than the SLR-only solution (0.06 cm). Maximum differences amount to 0.15 cm for the combined solutions and SLR-only, while DORIS-only reaches up to 0.22 cm. The combined solutions provide the most consistent performance in the normal direction and effectively limit large outliers. As in the other components, the chosen weighting setup does not produce significant differences.

All components benefit from the homogeneous DORIS network and the larger number of observations, with the radial direction showing the smallest deviations overall, whereas the SLR-only solution is the least stable in all three directions. This directional behavior is consistent with a previous orbit overlap study. Although Guo et al. (2010) analyze a completely different satellite mission and tracking configuration, they report the same directional pattern, with the smallest differences occurring in the radial direction, the largest in the transverse component, and intermediate deviations in the normal component.

Across all components, the combined DGFI-TUM solutions provide the most robust and homogeneous behavior. SLR-only performs weakest in the radial and transverse directions, while DORIS-only shows increased outliers in the normal direction. The two tested weighting combinations (d+s 0.2 5 and d+s 0.1 5) yield nearly identical results, indicating no clear preference for one over the other. Table 9 shows that combining SLR and DORIS observations improves the stability between consecutive arcs and reduces the magnitude of deviations between different arcs. Figure 14 shows the orbit overlaps for solution d+s 0.2 5. The 13 colors correspond to the 13 overlapping intervals based on the 14 arcs.

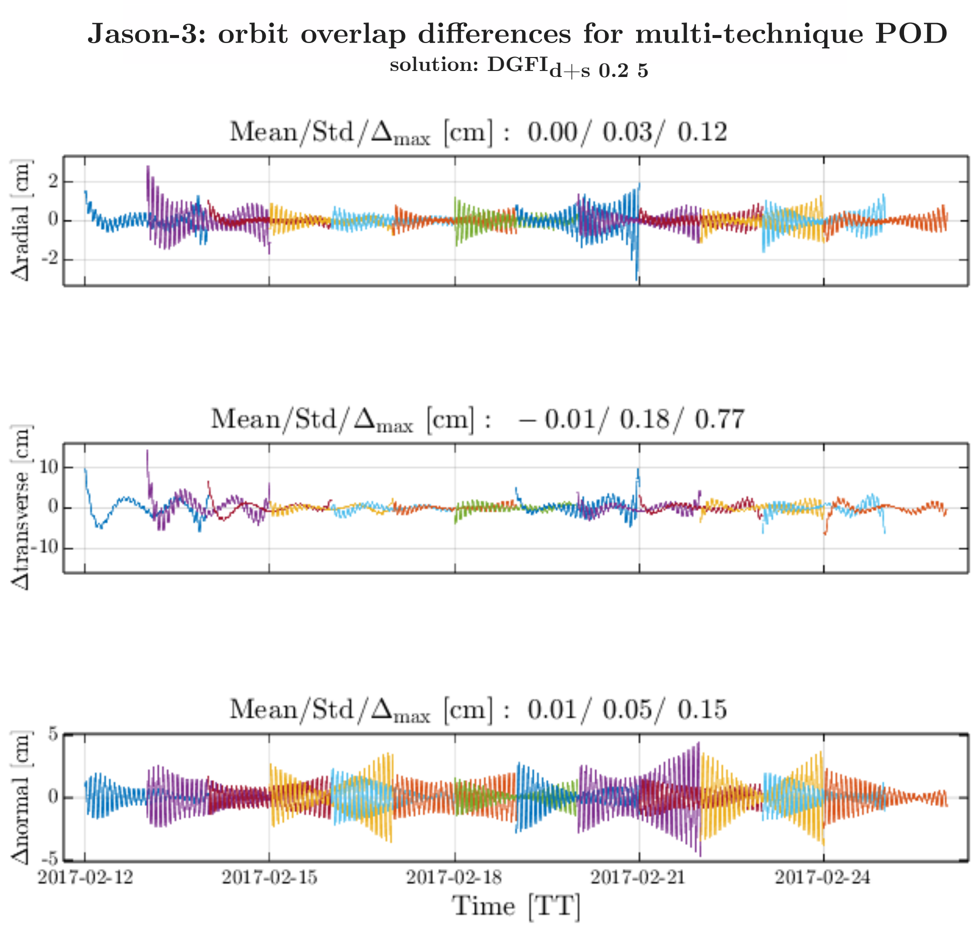

Figure 14 Orbit overlap differences for the DGFI solution d+s 0.2 5. Mean, standard deviation, and maximum differences are given as numerical values, while the overlaps are shown visually.

4.2 External validation

As noted in Section 4.1.3, the d+s 0.35 3 solution exhibits an a posteriori variance factor closer to one, but shows larger deviations from the reference orbit. The corresponding values are listed in Table 10. Due to these large deviations, this solution was not considered as the best setup.

Table 10 Solutions with smaller a posteriori variance factors (d+s 0.35 1 and d+s 0.35 3), showing the standard deviation, mean, and median of the orbit differences with respect to the SSA orbit.

	Radial [cm]			Transverse [cm]			Normal [cm]		
Solution	**Std. dev.**	**Mean**	**Median**	**Std. dev.**	**Mean**	**Median**	**Std. dev.**	**Mean**	**Median**
(1) JPL_{poe}	0.45	-0.15	-0.13	0.79	-0.12	-0.11	0.72	0.04	0.01
(2) $\text{DGFI}_{d+s\ 0.35\ 1}$	0.88	0.02	0.01	2.71	0.54	0.67	1.43	0.12	0.12
(3) $\text{DGFI}_{d+s\ 0.35\ 3}$	0.81	0.01	0.00	2.47	0.65	0.71	1.38	0.14	0.15

For external validation, the combined d+s 0.2 5 and d+s 0.1 5 solutions, along with their respective single-technique solutions, are used. The first part of Table 11 lists solution differences with respect to the JPL_{poe} orbit. The first entry, (1), shows the differences between the $SSA_{POE\text{-}F}$ and the JPL_{poe} orbit and serves as the reference comparison, representing the target range to be approached, as this reflects an achievable difference between two external orbits.

The comparisons (2) and (3) represent the best-performing DGFI-TUM solutions with respect to the JPL orbit. They use the weighting settings defined in Chapter 3.4 (see Table 7), with σ_{sys} values of 0.2 mm/s for DORIS and 5 cm for SLR in solution (2), and 0.1 mm/s for DORIS and 5 cm for SLR in solution (3). The comparisons (4)-(6) show the respective single-technique solutions with respect to the JPL orbit: (4) with DORIS-only and 0.2 mm/s, (5) with DORIS-only and 0.1 mm/s and (6) with SLR-only and 5 cm, each with respect to the JPL orbit.

Table 11 Best setups for σ_{sys}, showing the standard deviation, mean, and median of orbit differences with respect to the JPL orbit (upper part) and the SSA orbit (lower part). The table presents the best multi-technique setups, along with their corresponding single-technique solutions, and highlights the best-performing setup in each section.

	Radial [cm]			Transverse [cm]			Normal [cm]		
Solution	**Std. dev.**	**Mean**	**Median**	**Std. dev.**	**Mean**	**Median**	**Std. dev.**	**Mean**	**Median**
(1) $SSA_{POE\text{-}F}$	0.45	0.15	0.13	0.79	0.12	0.10	0.72	-0.04	-0.01
(2) $DGFI_{d+s\ 0.2\ 5}$	0.73	0.15	0.14	2.36	0.82	0.94	1.17	0.12	0.10
(3) $DGFI_{d+s\ 0.1\ 5}$	0.73	0.15	0.16	2.39	0.83	0.94	1.29	0.11	0.10
(4) $DGFI_{DORIS-only\ 0.2}$	0.74	0.15	0.14	2.45	0.80	0.92	1.57	0.13	0.10
(5) $DGFI_{DORIS-only\ 0.1}$	0.73	0.15	0.14	2.42	0.81	0.92	1.57	0.12	0.10
(6) $DGFI_{SLR-only\ 5}$	0.83	0.16	0.15	2.79	0.66	0.71	1.24	0.10	0.09
(1) JPL_{poe}	0.45	-0.15	-0.13	0.79	-0.12	-0.11	0.72	0.04	0.01
(2) $DGFI_{d+s\ 0.2\ 5}$	0.74	0.01	-0.01	2.39	0.71	0.89	1.30	0.15	0.16
(3) $DGFI_{d+s\ 0.1\ 5}$	0.72	0.01	0.00	2.41	0.72	0.87	1.41	0.15	0.15
(4) $DGFI_{DORIS-only\ 0.2}$	0.72	0.00	-0.01	2.46	0.69	0.89	1.70	0.16	0.17
(5) $DGFI_{DORIS-only\ 0.1}$	0.72	0.00	-0.01	2.43	0.70	0.86	1.70	0.15	0.16
(6) $DGFI_{SLR-only\ 5}$	0.93	0.01	0.00	2.89	0.55	0.61	1.41	0.13	0.15

The standard deviation and mean values in the radial direction of the two DGFI-TUM solutions show the same values, with similar median values. In the transverse direction, the standard deviations differ slightly (2.36 cm for comparison (2) and 2.39 cm for (3)), with major differences in the normal direction (1.17 cm for comparison (2) and 2.29 cm for (3)). Because the orbit differences in comparison (2) are smaller than the values of comparison (3) with respect to the SSA orbit, comparison (2) exhibits the smallest deviation and therefore provides the best fit to the reference solution. The best-performing DGFI solution differences with respect to the SSA orbit are highlighted in green in Table 11.

The second part of the table presents the deviations of the DGFI-TUM solutions with respect to the SSA orbit. A similar behavior as in the JPL comparison can be observed: the multi-technique solution $DGFI_{d+s\ 0.1\ 5}$ shows smaller deviations in the radial direction, whereas $DGFI_{d+s\ 0.2\ 5}$ provides the closer agreement in the transverse and normal components. Only considering radial direction, the mean and median of the combined DGFI-TUM solutions with respect to the SSA orbit match the values from the JPL orbit to the SSA orbit. The mean and median in the other directions also match the SSA orbit more closely, but the standard deviation is higher compared to the difference from the JPL orbit.

The comparisons of the single-technique solutions (4)-(6) show that DORIS-only solutions match the JPL and SSA orbit better than the SLR-only solution. Although the DORIS-only solutions show a good agreement in radial direction, their standard deviations deviate more from the reference in transverse and normal directions. Additionally, for the single-technique solution, it is noted that the mean and median of the differences to the SSA orbit are smaller compared to JPL, but have a higher standard deviation. As the DGFI-TUM solutions for the 14 arcs better match the CNES POE-F solution, the SSA orbit is used as the reference orbit. The results for the external validation are shown in Figure 11c. Overall, an offset can be seen in the different mean and median values of the DGFI solutions relative to the JPL solutions. The DGFI solutions match the SSA solution more closely, as their mean and median values are close to zero, whereas the deviation from the JPL orbit is about 1.5 mm in both mean and median.

According to Koch (1999), the variance σ^2 is a measure of the dispersion of a random variable about its expected value. Consequently, the standard deviation σ, as the square root of the variance, can be interpreted as a measure of the average deviation of a random variable from its expected value, expressed in the same units as the variable itself. In this context, a larger standard deviation indicates a greater dispersion of the orbit differences, i.e., less consistency between the compared solutions. The mean represents the systematic offset of one orbit with respect to the reference, while the median provides a robust estimate of the central tendency, being less affected by outliers. A small difference between the mean and median, therefore, suggests a stable and symmetric distribution of the orbit differences.

The standard deviations in the radial direction show smaller values for the different orbit solution differences. The combined DGFI-TUM solutions exhibit standard deviations that are about 1.6 times larger with respect to the JPL and SSA orbits than the differences between the SSA and JPL orbits and the reference. In the transverse direction, the scatter is roughly three times larger than the corresponding reference value. For the normal direction, the standard deviations are between 1.6 and 1.9 times larger. The DORIS-only solutions show a similar behavior, whereas the SLR-only solutions exhibit larger values in all directions except the normal direction.

A small dispersion between solutions in the radial direction is particularly desirable because differences in the radial direction of altimetry satellites directly affect the estimated sea-surface height (Rudenko et al., 2023).

A previous study of Kong et al. (2017), which combined SLR and DORIS observations for the POD of the HY-2A satellite, reported that satellite orbits generally show a higher consistency in the radial direction compared to the transverse and normal components. Although the study focuses on HY-2A and covers a different time period, the authors do not provide details on their parameter setup and only state that a CNES reference orbit is used, without further specification. Despite these differences, the reported pattern is consistent with the tendency observed here: the radial component shows the closest agreement with the reference orbit, while the transverse and normal components exhibit larger deviations.

Figure 15 presents the orbit differences relative to the CNES $\mathrm{SSA}_{\text{POE-F}}$ solution for the best DGFI-

TUM multi-technique solution (with standard deviations of 0.2 mm/s for DORIS and 5 cm for SLR), as well as for the JPL_{poe} solution.

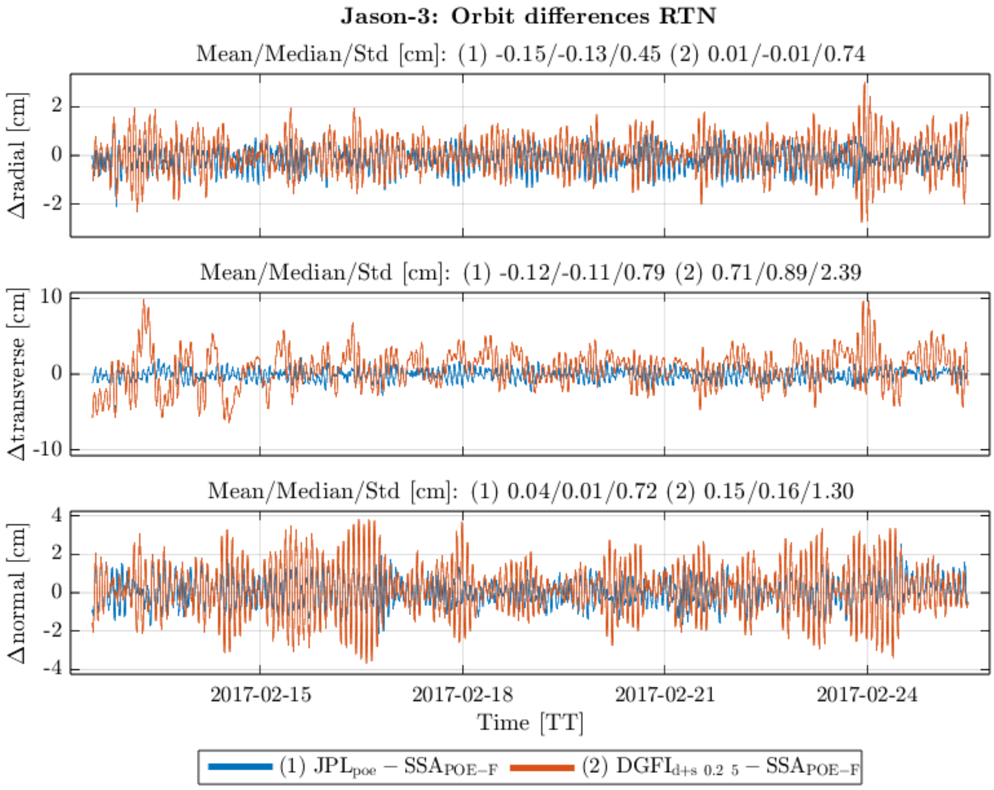

Figure 15 Orbit differences of DGFI-TUM and JPL solutions with respect to $SSA_{POE\text{-}F}$ solution.

There is another external orbit available from GSFC, called std2400 solution, combining DORIS and SLR observations (F. G. Lemoine et al., 2025). Because the solution was released in the final stage of this thesis, it is used here as an additional comparison. Figure 16 also includes the deviation of $GSFC_{std2400}$ to the SSA orbit, since among the available external solutions, the DGFI-TUM solution shows the closest agreement with the SSA orbit.

The reference difference of the JPL_{poe} solution with respect to the $GSFC_{std2400}$ solution shows a standard deviation of 0.71 cm in radial direction with a mean of -1.4 mm and median 1.7 mm, whereas the SSA solution better agrees with $GSFC_{std2400}$, shown by a standard deviation of 0.64 and mean and median values of 0.1 mm. The $DGFI_{d+s\ 0.2\ 5}$ solution has a standard deviation of 0.85 cm and a mean of 0.1 mm, a median of 0 cm, showing no offset regarding $GSFC_{std2400}$, but larger scattering. In the transverse and normal directions, the mean, median, and standard deviations increase, showing an offset and larger spreading of all three solutions with respect to $GSFC_{std2400}$. The solution $GSFC_{std2400}$ has different models, as described in F. G. Lemoine et al. (2025) and are not implemented according to POE-F standards. To obtain a genuine comparison, the applied models must be tailored to the setup of the DGFI-TUM solution. Due to time constraints, this adaptation was not performed.

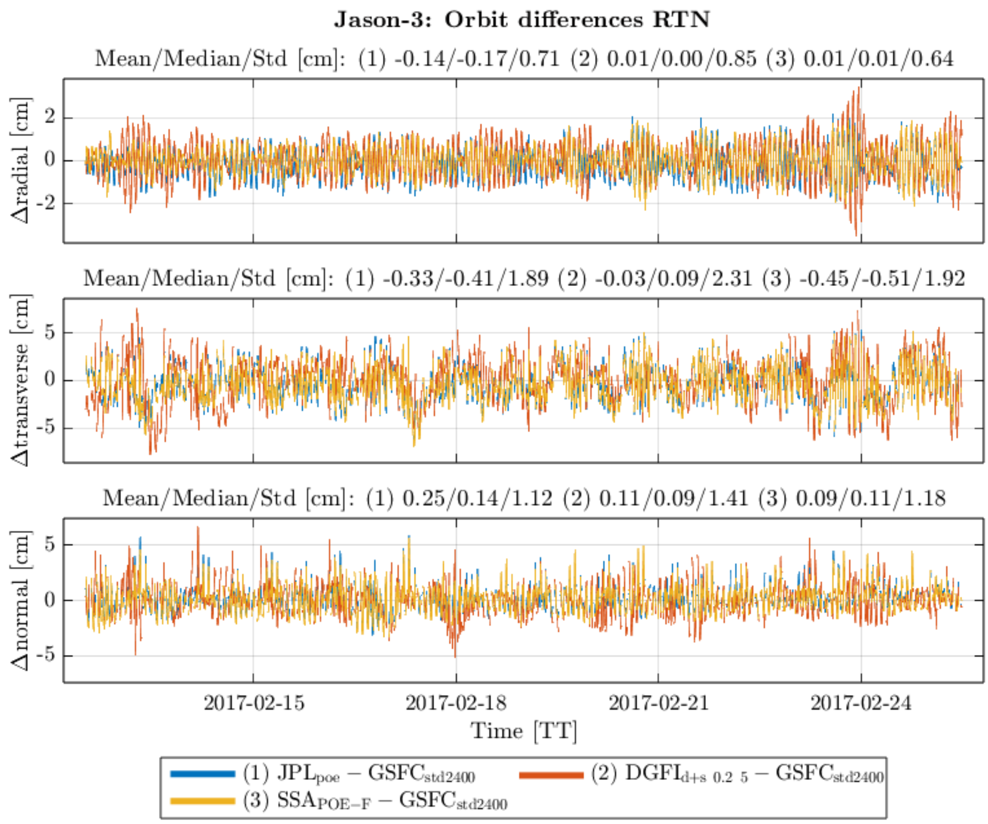

Figure 16 Orbit differences of JPL, DGFI-TUM and SSA solutions with respect to $GSFC_{std2400}$ solution.

In sum, it can be observed that the JPL_{poe} solution exhibits a radial offset of 1.5 mm relative to the SSA solution, which is also visible when comparing JPL_{poe} to $GSFC_{std2400}$. The radial differences in mean, median, and standard deviation are comparatively small. Still, the transverse and normal components show noticeably larger discrepancies, as indicated by increased mean, median, and standard deviation values. These elevated transverse and normal differences indicate an inconsistency in the realization of the DGFI-TUM solution with respect to the SSA solution and the cause of this inconsistency is currently unknown.

Comparison of POD results for the time span of the initial 200 arcs

The optimized settings derived from the third scenario, which comprises the 14 overlapping 3-day arcs, are applied to the entire time span covered by the 200 arcs of the first scenario to assess the improvement over the whole analysis period. This evaluation corresponds to scenario 4 in Figure 6 in Chapter 3.2. The following section presents the orbit differences with respect to the SSA orbit in terms of standard deviation, mean, and median. Table 12 provides the numerical values underlying Figure 17, including the comparisons of the external orbits (1) and (2), the initial setup (comparisons (3)–(5)), and the final setup (comparisons (8)–(9)), all relative to the SSA solution. The single-technique solutions (6) and (7) for the initial setup and (10)–(12) for the final setup are also listed to illustrate the benefit of the multi-technique solution. Comparisons (1) and (2) show how the external JPL_{poe} and $GSFC_{std2400}$ solutions differ from the SSA reference.

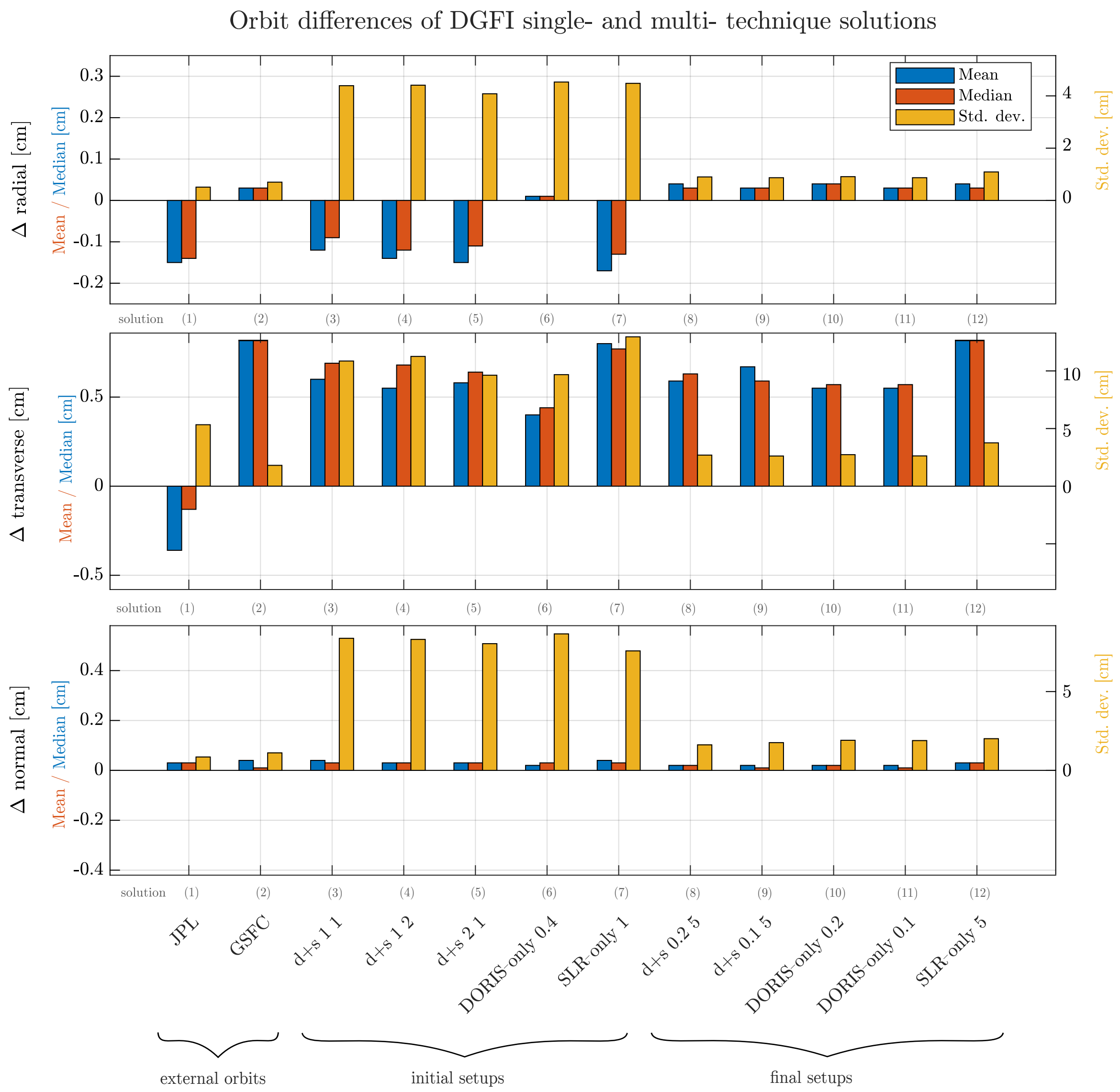

Figure 17 Orbit differences of various DGFI solutions with respect to the SSA orbit, showing mean, median, and standard deviation for the initial setup, final setups, and external orbits. Note the different scale of mean/median and standard deviation.

Comparison (1) serves as the reference comparison, representing the target range to be approached, as this is an achievable difference between two external orbits. For the initial setups (3)–(5) and the single-technique solutions (6)–(7), the σ_{sys} values are fixed to 0.4 mm/s for DORIS and 1 cm for SLR. The setups differ only in the choice of f_{typ}. The context for this parameter is given in Equation 3.1 in Section 3.2.2. The value of f_{typ} is either 1 or 2, consistent with the naming of the corresponding solutions and as described in Chapter 3, e.g., DGFI$_{d+s\,1\,2}$ assigns 1 to DORIS and 2 to SLR.

For the first scenario, comparison (5) yields the best performance and is therefore used to quantify the improvement across the different scenarios. For the final setup, comparison (9) shows the closest agreement with the reference solution SSA in the radial direction (std. dev. 8.7 mm) and in the transverse direction (std. dev. 2.68 mm), whereas comparison (8) agrees best in the normal direction (std. dev. 1.62 mm).

In contrast, comparison (1), representing the JPL orbit with respect to SSA, exhibits a markedly larger standard deviation in the transverse direction (5.46 cm) than the DGFI solution in comparison (8). This confirms the previously noted offset of the JPL orbit relative to SSA, as reflected not only in the standard deviation but also in the deviations of the mean and median values.

Table 12 Initial and final setup, showing the mean, median, and standard deviation of orbit differences with respect to the SSA orbit. The best initial setup and the two combined final setups are highlighted in the table.

	Radial [cm]			Transverse [cm]			Normal [cm]		
Solution	**Mean**	**Median**	**Std. dev.**	**Mean**	**Median**	**Std. dev.**	**Mean**	**Median**	**Std. dev.**
(1) $\mathrm{JPL}_{\mathrm{poe}}$	-0.15	-0.14	0.51	-0.36	-0.13	5.46	0.03	0.03	0.85
(2) $\mathrm{GSFC}_{\mathrm{std2400}}$	0.03	0.03	0.70	0.91	0.98	1.85	0.04	0.01	1.11
(3) $\mathrm{DGFI}_{d+s\ 1\ 1}$	-0.12	-0.09	4.39	0.60	0.69	11.12	0.04	0.03	8.38
(4) $\mathrm{DGFI}_{d+s\ 1\ 2}$	-0.14	-0.12	4.41	0.55	0.68	11.53	0.03	0.03	8.31
(5) $\mathrm{DGFI}_{d+s\ 2\ 1}$	-0.15	-0.11	4.08	0.58	0.64	9.86	0.03	0.03	8.04
(6) $\mathrm{DGFI}_{DORIS-only\ 0.4}$	0.01	0.01	4.53	0.40	0.44	9.91	0.02	0.03	8.66
(7) $\mathrm{DGFI}_{SLR-only\ 1}$	-0.17	-0.13	4.48	0.80	0.77	13.27	0.04	0.03	7.58
(8) $\mathrm{DGFI}_{d+s\ 0.2\ 5}$	0.04	0.03	0.90	0.59	0.63	2.76	0.02	0.02	1.62
(9) $\mathrm{DGFI}_{d+s\ 0.1\ 5}$	0.03	0.03	0.87	0.67	0.59	2.68	0.02	0.01	1.76
(10) $\mathrm{DGFI}_{DORIS-only\ 0.2}$	0.04	0.04	0.91	0.55	0.57	2.80	0.02	0.02	1.91
(11) $\mathrm{DGFI}_{DORIS-only\ 0.1}$	0.04	0.04	0.91	0.55	0.57	2.80	0.02	0.02	1.91
(12) $\mathrm{DGFI}_{SLR-only\ 5}$	0.04	0.03	1.09	0.88	0.91	3.85	0.03	0.03	2.01

To quantify the improvements across scenarios, the initial and final setups are compared in terms of their resulting orbit differences. Considering the standard deviation, the overall improvement of the DGFI solutions with respect to SSA can be described as follows:

In radial direction, for the initial setup, the best solution, meaning the smallest mean, median, and standard deviation values, with respect to SSA, is the $\mathrm{DGFI}_{d+s\ 2\ 1}$ solution with a standard deviation of 4.08 cm. This is a factor of 8 worse than the reference comparison, which is JPL with respect to SSA (standard deviation 0.51 cm). For the final setup, $\mathrm{DGFI}_{d+s\ 0.1\ 5}$ yields 0.87 cm, having only a factor 1.7 worse than the reference. Overall, there is a 3.6 mm difference in standard deviation for the radial direction left. The mean and median differences also agree now with 0.3 mm each, showing minor differences from the initial setup (-1.5 mm mean and -1.1 mm median).

In the transverse direction, the initial setup $\mathrm{DGFI}_{d+s\ 2\ 1}$ started with a standard deviation difference of 9.86 cm with respect to SSA (factor 1.8 worse). For the final setup, $\mathrm{DGFI}_{d+s\ 0.1\ 5}$ now shows a standard deviation of 2.68 cm. The reference comparison of JPL to SSA has a standard deviation of 5.46 cm, corresponding to a factor of 0.49 improvement in standard deviation of $\mathrm{DGFI}_{d+s\ 0.1\ 5}$ with respect to SSA than JPL to SSA.

In the normal direction, the reference comparison yields a standard deviation of 0.85 cm. The initial solution $\mathrm{DGFI}_{d+s\ 2\ 1}$ shows a substantially larger standard deviation of 8.04 cm, corresponding to a degradation by a factor of 9.5. For the final setup, the DGFI $_{d+s\ 0.1\ 5}$ solution is closer to the reference, with a standard deviation of 1.62 cm, while $\mathrm{DGFI}_{d+s\ 0.2\ 5}$ results in 1.76 cm. This means that $\mathrm{DGFI}_{d+s\ 0.1\ 5}$ is closer to the reference in the radial and transverse directions, whereas

DGFI$_{d+s\ 0.2\ 5}$ performs better in the normal direction. The differences may arise from changes in the setup of the σ_{sys} values between the solutions. However, this requires further investigation in future analyses.

The listed single-technique solutions also show improvements in all components between the initial and final setups, mostly because of the adaptation to the POE-F standards and the setup including overlapping arcs and the central day extracted. They are included to illustrate the potential enhancement achieved by the multi-technique solutions with respect to the SSA orbit. For the initial setup, comparisons (6) and (7) reveal that the DGFI$_{\text{DORIS-only}\ 0.4}$ solution exhibits smaller standard deviation and mean/median values than DGFI$_{\text{SLR-only}\ 1}$. The mean and median in the normal direction are nearly identical, while the standard deviation of DGFI$_{\text{DORIS-only}\ 0.4}$ is smaller in radial and transverse direction than that for DGFI$_{\text{SLR-only}\ 1}$, as expected due to the DORIS network geometry and the significantly larger number of observations. In the normal direction, the standard deviation of DGFI$_{\text{SLR-only}\ 1}$ (7.58 cm) and DGFI$_{\text{DORIS-only}\ 0.4}$ (8.66 cm) are nearly equal.

For the final setup, the respective single-technique solutions in comparisons (10) and (11), representing DORIS-only results, show larger standard deviations with respect to SSA than the combined solutions listed in comparisons (8) and (9). In the initial setup, some single-technique solutions exhibit smaller standard deviations than the combined solutions. For example, the standard deviation in the transverse direction for the DORIS-only solution (6) with respect to SSA is 9.91 cm, whereas the standard deviation of the combined solution (3) is 2 cm larger. The mean and median values of comparison (6) also tend to be closer than those of comparison (3). This behavior is attributed to the weighting settings used in the initial setups, which served as a starting point for the multi-technique POD, as they are established from single-technique settings. While σ_{sys} of 0.4 mm/s for DORIS and 1 cm for SLR perform well in a single-technique POD, they are not optimal for multi-technique POD.

The single-technique solutions additionally serve to assess the improvement achieved by the multi-technique solutions with respect to external references. The results show that the multi-technique solutions exhibit better agreement with external solutions than the corresponding single-technique solutions. Although DORIS-only benefits from a large number of observations, the combined solutions benefit from the combination with SLR with respect to the comparison with other solutions, resulting in smaller differences between the multi-technique solutions and the external reference orbits.

Overall, the analysis presented in this thesis demonstrates improvements in the deviation of the DGFI solutions relative to the external orbits, as measured by standard deviation, mean, and median. These improvements arise from refinements in the parameter estimation setup, the application weighting, and changes in the background models to meet the POE-F standards.

5 Conclusion and outlook

In this thesis, an observation-level combination of SLR and DORIS observations for POD is carried out. Initial values for determining the optimal weighting setup for multi-technique POD at DGFI-TUM are 0.4 mm/s for DORIS and 1 cm for SLR, based on single-technique analyses (personal communication, M. Bloßfeld). The published values for multi-technique POD available in the literature report 0.2 mm/s and 15 cm for the combination of SLR and DORIS observations of the HY-2A satellite (Kong et al., 2017), while the POE-F standards describe 1.5 mm/s and 15 cm (Couhert et al., 2022). To determine an appropriate weighting for the multi-technique POD at DGFI-TUM, externally available orbits are used as a reference by comparing orbit differences between the DGFI-TUM setup, the JPL orbit, the SSA orbit, and the GSFC orbit.

To analyze the weighting-specific behavior of the different setups, 200 arcs are first computed using initial σ_{sys} values of 0.4 mm/s for DORIS and 1 cm for SLR. These values originate from single-technique solutions but show large deviations from external reference orbits. Therefore, an optimal set of technique-specific σ_{sys} values must be identified. For this purpose, 33 different configurations are tested for the first arc of the mission and evaluated against the JPL reference orbit. The optimal values for σ_{sys} are determined as 0.1 mm/s for DORIS and 5 cm for SLR when considering only the radial direction. A σ_{sys} setup of 0.2 mm/s for DORIS and 5 cm for SLR is the best setup when evaluated across all three directions and is used to find the best setup of the estimated parameters. Among the various tight-constrained and loose-constrained configurations, the parameter setup that shows the smallest mean and median deviations from the JPL orbit is the one in which the SRP and ALB parameters are treated as tightly constrained parameters, while all other parameters, including EMP in the transverse and normal directions, are handled as loosely constrained. Also, range bias, frequency bias, frequency drift, and the scaling factor of tropospheric refraction are estimated.

Additionally, 14 arcs with a high number of SLR observations are selected to verify the derived standard deviations (σ_{sys}) and their parameter setup. To improve the results of this experiment, each arc covers a three-day period with a one-day offset. Only the central day of each arc is analyzed to avoid boundary effects in the least-squares adjustment, since larger errors typically occur at the beginning and end of an arc. Also in this time span, the same σ_{sys} values for DORIS and SLR with respect to the reference orbit are obtained, confirming the previously derived weighting setup. For the 14 arcs, the DGFI-TUM solutions agree more with the SSA orbit than the JPL solution, which only agrees better with the DGFI-TUM solutions for the first arc of the mission. The external orbits are, primarily, used to determine the optimal weighting setup of a multi-technique POD. Therefore, the chosen models are according to POE-F standards. Applying the optimized configuration across the full time span of the initial 200 arcs confirms an overall improvement throughout the analysis period.

To validate the orbit solution, both internal and external validation are performed. Internal validation includes the analysis of the estimated parameters and an orbit overlap analysis, while the external validation is based on orbit differences with the JPL, SSA, and GSFC solutions. The different DGFI solutions show similar behavior in the estimated parameters, statistical measures, and orbit overlap differences, but the $\mathrm{DGFI}_{\mathrm{d+s}\,0.2\,5}$ solution exhibits the smallest deviations in the orbit differences with respect to the JPL and SSA products and is therefore considered the best setup. The GSFC orbit was published in the final stage of this thesis, but the comparison is included to provide an additional reference using the same technique setup. Since the GSFC solution does not follow the POE standards (F. G. Lemoine et al., 2025), a full comparison would require adapting the DGFI setup accordingly, a step that could not be realized within the time constraints of this thesis.

Initially, the following research question was formulated:

> **How can SLR and DORIS observations be relatively weighted, and how should the parameter setup be chosen, to obtain a reliable satellite orbit solution?**

The best derived setup for multi-technique solution is 0.2 mm/s for DORIS and 5 cm for SLR, called solution $\mathrm{DGFI}_{\mathrm{d+s}\,0.2\,5}$, with the following parameter setup: SRP and ALB as tc setup (0.01) and the other estimated parameters are set up as lc (ATMO 1.0, EMP periodic 2.0 nm/s^2, EMP polygon 1.0 nm/s^2). The empirical accelerations, both periodic and polygonal, are estimated in the normal and transverse directions. Also, scaling parameters of tropospheric refraction, frequency bias, and range bias are estimated for all stations per pass. Frequency drift is estimated per station per arc.

All values are subject to change and may vary depending on the satellite type and mission period. For TOPEX, the time bias cannot be neglected (F. G. Lemoine et al., 2018), the derived setup could also be applied and computed for other satellites. For Jason-3, it is reasonable to compute values over the entire mission period, even in cases where only a limited number of observations are available. As an additional validation method, a crossover analysis over the full mission duration could be performed to assess orbit consistency at ground track intersections of ascending and descending passes.

Furthermore, a combination at the normal-equation level could be implemented. Instead of relying on static weighting values, a weekly variance component estimation would allow the weights to vary over time and, on average, achieve an a posteriori variance factor close to unity. Additionally, the correlations of the estimated parameters could be analyzed in future work.

Acronyms

A

ALB - Earth Albedo 25, 29, 41, 42, 57, 58
ATMO - Atmospheric drag 25, 29, 41, 42, 43, 58

B

BKG - Federal Agency for Cartography and Geodesy 3

C

CNES - Centre National d'Études Spatiales 8, 12, 13, 15, 31, 37, 51

D

DGFI-TUM - Deutsches Geodätisches Forschungsinstitut 1, 3, 4, 20, 23, 24, 25, 33, 34, 37, 39, 42, 47, 48, 50, 51, 52, 53, 57, 61, 62
DLR - German Aerospace Center 3
DOGS - DGFI orbit and geodetic parameter estimation software 24
DOGS-OC - DGFI orbit and geodetic parameter estimation software - orbit computation..... 14, 24, 25, 26, 28, 29, 30, 35, 39
DORIS - Doppler Orbitography and Radiopositioning Integrated by Satellite .. 1, 2, 3, 4, 5, 8, 9, 10, 11, 12, 13, 15, 16, 19, 20, 21, 22, 23, 25, 26, 27, 29, 30, 31, 33, 34, 37, 39, 41, 43, 44, 45, 46, 47, 48, 50, 51, 52, 54, 56, 57, 58, 61
DPOD2020 - DORIS extension of the ITRF for Precise Orbit Determination 8, 26
DTRF2020 - The ITRS2020 realization of DGFI-TUM 1

E

EMP - Empirical Accelerations 25, 29, 41, 42, 43, 57, 58
EOP - Earth Orientation Parameters 26
ESA - European Space Agency 2, 3
EUMETSAT - European Organisation for the Exploitation of Meteorological Satellites 12

G

GFZ - German Research Centre for Geosciences 3
GGOS - Global Geodetic Observing System 2, 11
GNSS - Global Navigation Satellite System 1, 2, 3, 9, 11, 15
GPS - Global Positioning System 3, 12, 13, 29, 37
GRGS - Groupe de Recherche de Géodésie Spatiale 8
GSFC - Goddard Space Flight Center 15, 37, 52, 57, 58

I

IAG - International Association of Geodesy 1, 2
IDS - International DORIS Service 8, 10, 16

IERS - International Earth Rotation and Reference Systems Service 1, 26
IGN - Institut national de l’information géographique et forestière 1, 8
ILRS - International Laser Ranging Service 5, 7, 30
ITRF - International Terrestrial Reference Frame 1, 2, 5, 10, 24, 26
ITRS - International Terrestrial Reference System 1
IUGG - International Union of Geodesy and Geophysics 1

J

JPL - Jet Propulsion Laboratory 1, 15, 31, 32, 33, 37, 41, 50, 51, 52, 53, 57, 58, 61, 62
JTRF2020 - JPL Terrestrial Reference Frame 2020 1

L

lc - loose-constrained 29, 30, 31, 33, 39, 58
LLR - Lunar Laser Ranging 5

N

NASA - National Aeronautics and Space Administration 5, 12, 13, 15
NOAA - National Oceanic and Atmospheric Administration 12

P

POD - Precise orbit determination ... 2, 3, 4, 5, 8, 13, 15, 16, 20, 22, 23, 24, 25, 26, 27, 29, 30, 31, 33, 34, 39, 51, 53, 56, 57, 61, 62
POE - Precise orbit ephemeris 15, 26, 31, 50, 52, 56, 57, 58

R

RMS - root mean square 4, 9, 35, 45

S

SLR - Satellite Laser Ranging. 1, 2, 3, 4, 5, 6, 7, 8, 9, 11, 12, 13, 15, 19, 20, 21, 22, 23, 25, 26, 27, 28, 29, 30, 31, 33, 34, 37, 39, 41, 43, 44, 45, 47, 48, 50, 51, 52, 54, 56, 57, 58, 61
SLRF2020 - Satellite Laser Ranging Frame 2020 .... 8, 26
SRP - Solar radiation pressure 25, 29, 41, 57, 58
SSALTO - Segment Sol multi-mission Altimétrie, Orbitographie et Localisation Précise 9, 10

T

tc - tight-constrained 29, 30, 31, 33, 58

U

USO - Ultra Stable Oscillator 3, 9

V

VLBI - Very Long Baseline Interferometry 1, 2, 3, 9

List of Figures

1 Schematic overview of SLR measurement principle, illustration based on Lösler et al. (2021) and Zeitlhöfler (2019), modified by the author. Satellite image taken from NASA Goddard Space Flight Center (1976). 6
2 Global distribution of SLR stations and DORIS beacons. 8
3 Schematic overview of DORIS segments and measurement principle, illustration based on CNES (2023). 9
4 Functional principle of the Jason-3 satellite mission (NASA et al., 2020). 13
5 Workflow for determining and validating the optimal weighting setup for multi-technique POD. 23
6 Test scenarios for determining the optimal σ_{sys} in multi-technique POD. Orange boxes denote experiment steps, red boxes indicate the time span in GPS weeks and the corresponding day of week, and green boxes represent outputs for subsequent processing. 27
7 Number of SLR observations for 200 arcs, highlighting the chosen 14 arcs in orange. 28
8 Handling of maneuvers in the first and last test scenario, with (a) showing the 3.5-day arc configuration (adapted from Zeitlhöfler (2019)) and (b) the 3-day consecutive overlapping arcs. 28
9 Technique-specific standard deviations in the context of multi-technique POD, illustrating standard deviation, mean, and median differences with respect to the JPL reference orbit in the radial component. 32
10 Internal and external orbit validation for consecutive 3-day arcs starting one day apart (start day d), showing orbit overlaps (green) and orbit differences to external orbits (purple). 34
11 Average values of physical and statistical parameters of the best multi-technique DGFI-TUM solutions, shown in comparison with the respective single-technique solutions, including internal and external validation (with respect to the SSA orbit). 42
12 Frequency bias [Hz] and range bias [cm] differences per station, sorted by number of observations (descending). 44
13 Comparison of a posteriori variance factors between multi-technique and corresponding single-technique solutions. 46
14 Orbit overlap differences for the DGFI solution d+s 0.2 5. Mean, standard deviation, and maximum differences are given as numerical values, while the overlaps are shown visually. 49
15 Orbit differences of DGFI-TUM and JPL solutions with respect to $\text{SSA}_{\text{POE-F}}$ solution. . 52

16 Orbit differences of JPL, DGFI-TUM and SSA solutions with respect to $GSFC_{std2400}$ solution. 53
17 Orbit differences of various DGFI solutions with respect to the SSA orbit, showing mean, median, and standard deviation for the initial setup, final setups, and external orbits. Note the different scale of mean/median and standard deviation. 54

List of Tables

1 Key mean orbital parameters of Jason-3 (NASA et al., 2020). 12
2 General settings for multi-technique POD. 24
3 Maneuvers occurring within the time span of the 200 arcs (Scenario 4). 29
4 Overview of the perturbation modeling scenarios and applied a priori standard deviations. N denotes the normal direction and T the transverse direction. 30
5 Parameter setup testing for multi-technique POD (σ_{sys} 0.2 mm/s (DORIS) and 5 cm (SLR)) showing standard deviation, mean, and median of orbit differences with respect to the JPL orbit, with the best-performing parameter setup highlighted. 33
6 External single- and multi-technique orbits. 37
7 Setup of technique-specific standard deviations, a priori standard deviations, and estimated biases for multi-technique POD. 39
8 Mean values of estimated biases for each combined solution (d+s 0.2 5 and d+s 0.1 5) and their corresponding single-technique solutions. 43
9 Statistical comparison of orbit overlaps for different DGFI solutions (d+s 0.2 5 and d+s 0.1 5) with their corresponding single-technique solutions, including the mean, standard deviation, and maximum absolute differences per direction (cm). 47
10 Solutions with smaller a posteriori variance factors (d+s 0.35 1 and d+s 0.35 3), showing the standard deviation, mean, and median of the orbit differences with respect to the SSA orbit. 49
11 Best setups for σ_{sys}, showing the standard deviation, mean, and median of orbit differences with respect to the JPL orbit (upper part) and the SSA orbit (lower part). The table presents the best multi-technique setups, along with their corresponding single-technique solutions, and highlights the best-performing setup in each section. . 50
12 Initial and final setup, showing the mean, median, and standard deviation of orbit differences with respect to the SSA orbit. The best initial setup and the two combined final setups are highlighted in the table. 55

Bibliography

Altamimi, Z., Rebischung, P., Collilieux, X., et al. (2023). ITRF2020: an augmented reference frame refining the modeling of nonlinear station motions. *Journal of Geodesy*, *97*(47). https://doi.org/10.1007/s00190-023-01738-w

Altamimi, Z., Rebischung, P., Métivier, L., & Collilieux, X. (2016). ITRF2014: A new release of the International Terrestrial Reference Frame modeling nonlinear station motions. *Journal of Geophysical Research: Solid Earth*, *121*(8), 6109–6131.

Altamimi, Z., & Seitz, F. (2025). ITRF and combination of techniques, system aspects session [Presentation at the Genesis Science Workshop, 2025, Matera, Italy].

Angermann, D., Seitz, M., Bloßfeld, M., & Seitz, F. (2024). Terrestrial reference frames: The fundament for geodetic earth observation and all positioning applications. *AVN Allgemeine Vermessungs-Nachrichten*, *2024*(5-6), 236–245. https://doi.org/10.14627/avn.2024.5-6.2

Angermann, D., Pail, R., Seitz, F., & Hugentobler, U. (2022). *Mission earth: Geodynamics and climate change observed through satellite geodesy*. Springer. https://doi.org/10.1007/978-3-662-64106-4

Auriol, A., & Tourain, C. (2010). DORIS system: The new age. *Advances in Space Research*, *46*(12), 1484–1496. https://doi.org/10.1016/j.asr.2010.05.015

AVISO. (2025a). *GPSP tracking receiver*. Retrieved September 3, 2025, from https://www.aviso.altimetry.fr/en/missions/current-missions/jason-3/instruments/gpsp.html

AVISO. (2025b). *Jason-3 ground system overview*. Retrieved August 29, 2025, from https://www.aviso.altimetry.fr/en/missions/current-missions/jason-3/ground-system.html

Bate, R. R., Mueller, D. D., & White, J. E. (1971). *Fundamentals of astrodynamics* (Reprint). Dover Publications.

Beutler, G., Schildknecht, T., Hugentobler, U., & Gurtner, W. (2003). Orbit determination in satellite geodesy. *Advances in Space Research*, *31*(8), 1853–1868. https://doi.org/10.1016/S0273-1177(03)00171-6

Bloßfeld, M. (2015). *The key role of Satellite Laser Ranging towards the integrated estimation of geometry, rotation and gravitational field of the Earth* [Doctoral dissertation, Technische Universität München]. https://mediatum.ub.tum.de/1231180

CDDIS. (2020). Nasa crustal dynamics data information system (cddis). https://cddis.nasa.gov/archive/doris/products/orbits/ssa/ja3/

Chen, L., Bai, X.-Z., & Li, K. (2017). Orbital prediction error propagation of space objects. In *Orbital data applications for space objects* (pp. 23–45). Springer Nature Singapore / National Defense Industry Press. https://doi.org/10.1007/978-981-10-2963-9_2

CNES. (2018). POD Configuration POE-F [Technical report].

CNES. (2023). *Doris system definition*. Retrieved July 18, 2025, from https://ids-doris.org/documents/BC/DORIS_System_Definition.pdf

Combrinck, L. (2010). Satellite Laser Ranging. In G. Xu (Ed.), *Sciences of geodesy - I: Advances and future directions* (pp. 301–338). Springer. https://doi.org/10.1007/978-3-642-11741-1_9

Couhert, A., Moyard, J., Mercier, F., Houry, S., Braz, T., Debout, V., Katsigianni, G., Saquet, E., Desai, S., & Lemoine, F. G. (2022). CNES POE-F precise orbit performances for the Jason-3 and Sentinel-6 MF missions [Venice, Italy. Centre National d'Etudes Spatiales (CNES)].

Courde, C., et al. (2025). Working Group 5 SLR Session [Presentation at the Genesis Science Workshop, 2025, Matera, Italy].

Curtis, H. D. (2005). *Orbital mechanics for engineering students* (2nd ed.). Elsevier / Butterworth-Heinemann.

Degnan, J. J. (1993). Millimeter accuracy satellite laser ranging: A review. In D. E. Smith & D. L. Turcotte (Eds.), *Contributions of space geodesy to geodynamics: Technology* (pp. 133–162, Vol. 25). American Geophysical Union. https://doi.org/10.1029/GD025p0133

Delva, P., Altamimi, Z., Blazquez, A., Bloßfeld, M., Böhm, J., Bonnefond, P., Boy, J.-P., Bruinsma, S., Bury, G., Chatzinikos, M., Couhert, A., Courde, C., Dach, R., Dehant, V., Dell'Agnello, S., Elgered, G., Enderle, W., Exertier, P., Glaser, S., & Zajdel, R. (2025, January 24). *GENESIS: Co-location of geodetic techniques in space*. https://doi.org/10.48550/arXiv.2209.15298

Desai, S. D., Bertiger, W., Haines, B., & Sibois, A. (2020). Evaluation of the use of high rate tracking data for jason-3 gps-based precise orbit determination. https://ostst.aviso.altimetry.fr/fileadmin/user_upload/tx_ausyclsseminar/files/Desaietal_GPSP_POD_2020OSTST.pdf

Fusco, G., & Waller, P. (2025). Genesis mission status & key topics [Presentation at the Genesis Science Workshop, Matera, Italy].

GGOS, I. (2023). *The importance of geodetic reference frames*. Retrieved September 5, 2025, from https://geodesy.science/2023/importance-reference-frames/

GGOS, I. (2025). *Ggos global geodetic observing system*. Retrieved October 8, 2025, from https://geodesy.science/ggos/

Gidlund, S. (2024). Genesis mission status and objectives [Presentation at the GENESIS Science Workshop, European Space Operations Centre (ESOC), Darmstadt, Germany].

Gopalarathnam, A. (2015). *Orbit and uncertainty propagation for space object catalogue maintenance* [Doctoral dissertation, University of Colorado Boulder] [Available in institutional repository].

Gross, R., Abbondanza, C., Chin, M., Heflin, M., & Parker, J. (2023). JTRF2020: Results and Next Steps [23–28 April]. *EGU General Assembly 2023*. https://doi.org/10.5194/egusphere-egu23-2117

Guo, R., Hu, X., Tang, B., Huang, Y., Liu, L., Cheng, L., & He, F. (2010). Precise orbit determination for geostationary satellites with multiple tracking techniques. *Chinese Science Bulletin*, *55*(8), 687–692. https://doi.org/10.1007/s11434-010-0074-x

Honoré-Livermore, E. (2024). Genesis system, satellite and payload overview [Presentation at the GENESIS Science Workshop, European Space Operations Centre (ESOC), Darmstadt, Germany].

Hugentobler, U. (2024). Genesis – history & discussion points [Presentation at the GENESIS Science Workshop, European Space Operations Centre (ESOC), Darmstadt, Germany].

IAG. (2025). *Ilrs – international laser ranging service*. Retrieved August 29, 2025, from https://geodesy.science/item/ilrs/

IDS. (2025). *Station management*. Retrieved August 30, 2025, from https://ids-doris.org/resources/technical-documents.html?catid=38%3Astations&id=167%3Astation-management&view=article

IDS Data Center. (2020). *Doris RINEX implementation in GINS v2.0* (tech. rep.). International DORIS Service (IDS). Retrieved July 16, 2025, from https://ids-doris.org/documents/BC/data/DORIS_RINEX_implementation_in_GINS.v2.0.pdf

IERS. (2025). *Combined earth rotation parameter solution consistent with the international terrestrial reference frame (itrf) 2020* [Data set]. https://hpiers.obspm.fr/eoppc/eop/eopc04/eopc04.1962-now

ILRS. (2023). Data Handling File for the International Laser Ranging Service (ILRS) extension of the International Terrestrial Reference Frame 2020 (ITRF2020) TRF model with additional SLR sites [Accessed 2025-12-06]. https://doi.org/10.5067/SLR/SLRF_2020_DHF_001

ILRS. (2025). *Map of stations*. Retrieved July 4, 2025, from https://ilrs.gsfc.nasa.gov/network/stations/index.html

International DORIS Service. (2025). *Doris satellite models implemented in poe processing* [Technical report, CNES / IDS]. Retrieved November 17, 2025, from https://ids-doris.org/documents/BC/satellites/DORISSatelliteModels.pdf

International Union of Geodesy and Geophysics. (2007). *Resolution 2: Geocentric and International Terrestrial Reference Systems (GTRS and ITRS)*. Retrieved November 15, 2025, from https://cloud.geodesy.science/s/p67FR4mj8ngNjHS

Jayles, C., Nhun-Fat, B., & Tourain, C. (2006). DORIS: System description and control of the signal integrity. *Journal of Geodesy*, *80*, 457–472. https://doi.org/10.1007/s00190-006-0046-8

Johnston, G., Riddell, A., & Hausler, G. (2017). The International GNSS Service. In P. J. G. Teunissen & O. Montenbruck (Eds.), *Springer handbook of global navigation satellite systems* (1st ed., pp. 967–982). Springer International Publishing. https://doi.org/10.1007/978-3-319-42928-1

JPL. (2020). Jet populson laboratory [data set]. https://sideshow.jpl.nasa.gov/pub/usrs/jason3/jplgpspoe/

Koch, K.-R. (1999). *Parameter estimation and hypothesis testing in linear models* (2nd ed.). Springer.

Kong, Q., Guo, J., Sun, Y., Zhao, C., & Chen, C. (2017). Centimeter-level precise orbit determination for the hy-2a satellite using doris and slr tracking data. *Acta Geophysica*, *65*(1), 1–12. https://doi.org/10.1007/s11600-016-0001-x

Lemoine, F. G., Zelensky, N. P., Beckley, B. D., Mitchum, G. T., Yang, X., & Nicholas, J. B. (2025, September). *std2400 Precise Orbit Determination (POD) Standards* (tech. rep.). NASA Goddard Space Flight Center. Greenbelt, Maryland, USA. https://ids-doris.org/documents/BC/data/std2400_orbit_standards_DORIS+SLR_NASA_GSFC.pdf

Lemoine, F. G., Zelensky, N. P., Belli, A., Couhert, A., Moreaux, G., Saunier, J., & Ferrage, P. (2018). The synergy of satellite laser ranging (slr) and doris as space geodesy techniques [Presentation at 21st International Workshop on Laser Ranging, Canberra, Australia].

Lemoine, F., & Moreaux, G. (2021). Overview of products for doris.

Lemoine, J.-M., Biancale, R., Reinquin, F., Bourgogne, S., & Gégout, P. (2019). CNES/GRGS RL04 Earth gravity field models, from GRACE and SLR data. https://doi.org/10.5880/ICGEM.2019.010

Lemoine, J.-M., & Capdeville, H. (2006). A corrective model for jason-1 doris doppler data in relation to the south atlantic anomaly [Published online: 8 August 2006]. *Journal of Geodesy*, *80*, 507–523. https://doi.org/10.1007/s00190-006-0068-2

Lösler, M., Eschelbach, C., Klügel, T., & Riepl, S. (2021). Ilrs reference point determination using close range photogrammetry. *Applied Sciences*, *11*(6), 2785. https://doi.org/10.3390/app11062785

MathWorks, Inc. (2025). Rms – root mean square value [Accessed: 7 November 2025].

McCarthy, D. D., & Petit, G. (Eds.). (2004). *Iers conventions (2003)* (IERS Technical Note No. 32). International Earth Rotation and Reference Systems Service (IERS). Frankfurt am Main, Verlag des Bundesamts für Kartographie und Geodäsie. https://www.iers.org/IERS/EN/Publications/TechnicalNotes/tn32

Montenbruck, O., & Gill, E. (2000). *Satellite orbits: Models, methods, and applications*. Springer. https://doi.org/10.1007/978-3-642-58351-3

Moreaux, G., et al. (2025). Doris session working group 4 [Presentation at the Genesis Science Workshop, 2025, Matera, Italy].

Moreaux, G., Lemoine, F. G., Zelensky, N. P., Moyard, J., & Couhert, A. (2023). Dpod2020: A DORIS extension of the ITRF2020 for precise orbit determination. *Advances in Space Research*, *72*(11), 4625–4650. https://doi.org/10.1016/j.asr.2023.10.006

Moyard, J., Couhert, A., Mercier, F., Houry, S., Saquet, E., Katsigianni, G., Cherrier, M., & Banos-Garcia, A. (2023). Cnes preliminary poe-g precise orbit performances for the Sentinel-6 MF mission. *Ocean Surface Topography Science Team (OSTST) Meeting*. file:///mnt/data/POD2023-CNES_preliminary_POE-G_precise_obit_performances_for_the_Sentinel-6_MF_mission.pdf

NASA. (2025). *Jason-3*. Retrieved June 17, 2025, from https://sealevel.jpl.nasa.gov/missions/jason-3/summary

NASA, NOAA, EUMETSAT, CNES, & JPL. (2020). *Jason-3 products handbook* (tech. rep. No. Issue 2.6) (Accessed: 2025-08-29). NOAA; EUMETSAT; CNES; NASA; JPL. https://www.ncei.noaa.gov/sites/default/files/2021-01/Jason-3%20Products%20Handbook.pdf

NASA Goddard Space Flight Center. (1976). *Lageos: Laser geodynamic satellite*. Retrieved August 29, 2025, from https://lageos.gsfc.nasa.gov/

Niemeier, W. (2008). *Ausgleichungsrechnung* (2nd ed.). De Gruyter.

Nothnagel, A., Artz, T., Behrend, D., & Malkin, Z. (2017). International VLBI Service for Geodesy and Astrometry: Delivering high-quality products and embarking on observations of the next generation. *Journal of Geodesy*, *91*(7), 711–721. https://doi.org/10.1007/s00190-016-0950-5

Pavlis, E., & Luceri, V. (2022). *The ILRS contribution to ITRF2020* [Data set]. https://itrf.ign.fr/docs/solutions/itrf2020/The_ILRS_contribution_to_ITRF2020_description_2022.09.23.pdf

Pearlman, M. R., Degnan, J. J., & Bosworth, J. M. (2002). The International Laser Ranging Service. *Advances in Space Research*, *30*(2), 135–143. https://doi.org/10.1016/S0273-1177(02)00277-6

Pearlman, M. R., Noll, C. E., Pavlis, E. C., et al. (2019). The ILRS: approaching 20 years and planning for the future. *Journal of Geodesy*, *93*, 2161–2180. https://doi.org/10.1007/s00190-019-01241-1

Petit, G., & Luzum, B. (Eds.). (2010). *Iers conventions 2010* (IERS Technical Note No. 36). International Earth Rotation and Reference Systems Service (IERS). Frankfurt am Main, Verlag des Bundesamts für Kartographie und Geodäsie. https://iers-conventions.obspm.fr/conventions_material.php

Plag, H.-P., & Pearlman, M. (Eds.). (2009). *Global geodetic observing system: Meeting the requirements of a global society on a changing planet in 2020*. Springer Berlin Heidelberg. https://doi.org/10.1007/978-3-642-02687-4

Rudenko, S., Dettmering, D., Lemoine, J.-M., Bloßfeld, M., & Zeitlhöfler, J. (2025). Impact of earth's mean time-variable gravity field models on precise orbits of altimetry satellites [Manuscript in review]. *Surveys in Geophysics*.

Rudenko, S., Bloßfeld, M., Kehm, A., Zeitlhöfler, J., & Gerstl, M. (2024). *Manual vi for dogs-oc version 5.5: Dogs-oc – input format*. Deutsches Geodätisches Forschungsinstitut at the Technical University of Munich (DGFI-TUM).

Rudenko, S., Dettmering, D., Zeitlhöfler, J., Alkahal, R., Upadhyay, D., & Bloßfeld, M. (2023). Radial orbit errors of contemporary altimetry satellite orbits. *Surveys in Geophysics*, *44*, 705–737. https://doi.org/10.1007/s10712-022-09758-5

Seitz, M., Bloßfeld, M., Angermann, D., Glomsda, M., Rudenko, S., Zeitlhöfler, J., & Seitz, F. (2023). DTRF2020: ITRS 2020 realization of DGFI-TUM (data). https://doi.org/10.5281/zenodo.8220524

Sośnica, K., Jäggi, A., Meyer, U., Thaller, D., Beutler, G., Arnold, D., & Dach, R. (2015). Time variable earth's gravity field from slr satellites. *Journal of Geodesy*, *89*(10), 945–960. https://doi.org/10.1007/s00190-015-0825-1

United Nations General Assembly. (2015). A global geodetic reference frame for sustainable development [Resolution adopted by the General Assembly on 26 February 2015 (A/RES/69/266)]. *United Nations*.

UTA. (2025). *Space Geodesy Satellite Laser Ranging System (SGSLR)*. Retrieved August 29, 2025, from https://www.csr.utexas.edu/research/mgo/mgo-instrumentation/sgslr/

Vallado, D. A. (2013). *Fundamentals of astrodynamics and applications* (4th). Microcosm Press.

Vaze, P., Neeck, S., Bannoura, W., Green, J., Wade, A., Mignogno, M., Zaouche, G., Couderc, V., Thouvenot, E., & Parisot, F. (2010). The jason-3 mission: Completing the transition of ocean altimetry from research to operations. In R. Meynart, S. P. Neeck, & H. Shimoda (Eds.). https://doi.org/10.1117/12.868543

Vermaat, E., Degnan, J. J., Dunn, P. J., Noomen, R., & Sinclair, A. T. (1998). Satellite laser ranging, status and impact for WEGENER. *Journal of Geodynamics*, *25*(3), 195–212. https://doi.org/10.1016/S0264-3707(97)00036-7

Vespe, F., & Karatekin, O. (2025). Genesis science exploitation team [Presentation at the Genesis Science Workshop, Matera, Italy].

Willis, P., Lemoine, F. G., Moreaux, G., Soudarin, L., Ferrage, P., Ries, J., Otten, M., Saunier, J., Noll, C., Biancale, R., & Luzum, B. (2016). The International DORIS Service (IDS), Recent Developments in Preparation for ITRF2013. In *Iag symposia series* (pp. 631–639, Vol. 143). Springer. https://doi.org/10.1007/1345_2015_164

Zeitlhöfler, J. (2019). *Nominal and observation-based attitude realization for precise orbit determination of the jason satellites* [Master's Thesis]. Technical University of Munich, Deutsches Geodätisches Forschungsinstitut (DGFI-TUM).